Materials Today Chemistry 42 (2024) 102375

Contents lists available at ScienceDirect

Materials Today Chemistry

journal homepage: www.journals.elsevier.com/materials-today-chemistry/

Anti-biofilm efficacy of novel silica-based nanoparticles functionalized with natural derivatives for surface coating

Giulia Cazzaniga [a,b,1], Cristina Cattò [c,1], Matteo Mori [a], Patricia Hayes [d], Dan Yang [d], Nuwan H. Arachchi [d], Federica Villa [c], Francesca Cappitelli [c], Alice Melocchi [a], Lucia Zema [a], Stefania Crespi [e], Paul J. Molino [d,**], Stefania Villa [a,*], Arianna Gelain [a]

[a] University of Milan, Department of Pharmaceutical Sciences, via L. Mangiagalli 25, 20133, Milan, Italy
[b] University od Insubria, Department of Science and High Technology, via Valleggio 9, 22100, Como, Italy
[c] University of Milan, Department of Food, Environmental and Nutritional Sciences, via G. Celoria 2, 20133, Milan, Italy
[d] University of Wollongong, AIIM Facility, Intelligent Polymer Research Institute, Wollongong, NSW, 2522, Australia
[e] University of Milan, Department of Earth Sciences "Ardito Desio", via L. Mangiagalli 34, 20133, Milan, Italy

ARTICLE INFO

Keywords:
Biofilm
Anti-Biofilm strategies
p-aminosalicylic acid derivatives
p-aminocinnamic acid derivatives
Inorganic nanoparticles

ABSTRACT

Biofilms colonize both biotic and abiotic surfaces, including living tissues, medical devices, water supply systems, and food processing equipment, posing health risks and financial burdens. In the present study, inorganic nanoparticles were functionalized with *p*-aminosalicylic acid or *p*-aminocinnamic acid, both established anti-biofilm agents at non-lethal concentrations. The final aim was to obtain new nanosystems for surface covering, mitigating the drawbacks associated with current antifouling coatings and tackling the pressing issue of antimicrobial resistance. Two series of silica nanoparticles were synthesized and characterized; the one with the highest degree of functionalization was selected for coating glass coverslips. The anti-biofilm properties of the resulting surfaces were tested against *Pseudomonas aeruginosa* biofilm. All coated surfaces showed a significant reduction in biofilm formation compared to the untreated controls, with a decrease ranging from -59.2 ± 2.2 to -83.7 ± 3.4. Importantly, the anti-biofilm coating did not affect the bacterial viability of both planktonic and sessile cells. Interestingly, the interaction between bacteria and the new surfaces led to an increase in bacterial metabolic activity, total protein amount, and oxidative stress levels. These findings indicate that the coatings affect biofilm formation by influencing bacterial physiology rather than simply killing the bacteria outright.

1. Introduction

Nearly all biotic and abiotic surfaces are susceptible to colonization by microbial biofilms, which are complex aggregations of microorganisms embedded in a self-produced extracellular polymeric matrix (EPM) [1]. Biofilms offer a favorable and cooperative environment for cells, protecting them from external harm. However, this very characteristic that benefits biofilm-dwelling cells can wreak havoc in medical and industrial settings, leading to serious health complications and significant economic costs. For instance, the National Institute of Health (NIH) estimates that most human microbial infections are either related to or directly provoked by bacterial biofilms [2], which display high tolerance to the currently approved FDA antibacterial drugs [3]. Based on recent estimates, the costs associated with unwanted biofilms reach nearly US$ 4 trillion annually, with approximately 400 billion for expenses related to human health [4].

Traditional strategies to control biofilm formation primarily focus on materials designed to kill microbial cells. However, these strategies have shown limited effectiveness due to the inherent tolerance of sessile bacteria, which can be up to 1000 times more resistant to biocides than their planktonic counterparts [5]. Therefore, the development of alternative strategies that sabotage the key steps of biofilm genesis (*e.g.*, attachment, cell-to-cell communication, dispersion) without killing the cells is highly desirable [6]. By exploiting mechanisms that do not exert selective pressure on microbial growth, we can potentially mitigate the emergence of drug-resistant mutations [7,8].

* Corresponding author. University of Milan, Department of Pharmaceutical Sciences, via L. Mangiagalli 25, 20133, Milan, Italy.
** Corresponding author. University of Wollongong, AIIM Facility, Intelligent Polymer Research Institute, Wollongong, NSW, 2522, Australia
E-mail address: stefania.villa@unimi.it (S. Villa).
[1] These authors contributed equally to this work.

https://doi.org/10.1016/j.mtchem.2024.102375
Received 5 August 2024; Accepted 26 October 2024
Available online 7 November 2024

In this context, our research group has identified natural compounds and developed novel materials that target biofilm formation pathways without harming cells. In a previous study [9], we have created innovative low-density polyethylene (LDPE)-based materials with anti-biofilm properties. Specifically, plasma-activated LDPE was covalently functionalized with two non-toxic natural derivatives, namely *p*-aminosalicylic acid and *p*-aminocinnamic acid. The resulting materials displayed remarkable anti-adhesion properties. When tested against *E. coli*, these newly developed materials significantly reduced biofilm formation (ranging from 50 to 80 %) without showing any toxicity towards the bacteria [9]. The mechanisms of action of *p*-aminosalicylic acid, *p*-aminocinnamic acid, and closely related structures have been deeply investigated in previous works. For example, zosteric acid, which shares the same active scaffold as *p*-aminocinnamic acid, has been shown to hinder cell adhesion to surfaces by altering the expression of various oxidative stress-related proteins [10]. Zosteric acid modulated the threshold level of AI-2 (autoinducer-2, a signal molecule) and induced a hypermotile phenotype in *E. coli*, preventing the bacterium from firmly adhering to surfaces [10]. Moreover, biofilms treated with salicylic acid showed increased levels of both intra- and extracellular ROS, leading to enhanced production of the quorum sensing signal indole. Furthermore, salicylic acid interacted with proteins that play a role in quorum sensing, ROS accumulation, motility, extracellular polymeric matrix components, transport, and metabolism [9]. A proteomic study identified the tryptophan [W]-repressor-binding protein (WrbA), an NADP:quinone oxidoreductase, as the main target of both *p*-aminosalicylic and *p*-aminocinnamic acids [11].

Although we previously covalently immobilized the active moieties of antibiofilm compounds on an LDPE surface [12], there is currently no established protocol for developing functionalized coatings that could be universally applied to any material. Therefore, building upon our previous understanding of anti-biofilm agents, our research aims to create a versatile and adaptable coating based on functionalized silica nanoparticles to effectively combat biofilm formation across a wide range of materials.

Silica nanoparticles offer useful applications across different domains, including advanced catalysis, drug delivery, biomedical applications, environmental remediation, and wastewater treatment [13–19].We chose Ludox HS-40, an alkaline colloidal silica characterized by small particle size, high binding strength, and stability, as our model coating agent due to its technological efficiency and versatility, which allows for different applications in various fields. For instance, a Ludox HS-40/sodium alginate biohybrid was developed for delivering doxorubicin, demonstrating effectiveness as a delivery system without causing cytotoxicity to healthy mouse lymphocytes [19]. Another study pointed out a positive effect of Ludox in reducing the *in vitro* toxicity of TiO_2:SiO_2 nanocomposites [20]. Moreover, a report by the European Centre for Ecotoxicology and Toxicology of Chemicals, as part of the Joint Assessment of Commodity Chemicals (JACC) program, highlighted the absence of skin reaction to Ludox HS-40 in a patch test performed on human volunteers [21]. Although further rigorous studies are needed, these data suggest that Ludox HS-40 could offer a good balance between technological properties and safety.

This paper describes the design, production, and analytical characterization of novel Ludox HS-40 nanoparticles functionalized with the anti-biofilm agents *p*-aminosalicylic acid and *p*-aminocinnamic acid [11,22,23]. The success of the synthetic process was verified using FT-IR, and Raman spectroscopy in combination with XPS and TGA. The resulting nanosystems were then employed to coat glass coverslips, which were used as representative model surfaces for broader material applications. These underwent extensive characterization using SEM, AFM, and other physical measurements. Finally, the anti-biofilm efficacy of the coated surfaces was assessed against the model bacterium *P. aeruginosa*, characterized by increased level of resistance towards multiple classes of antibiotics. Our promising results pave the way for the advancement and integration of these functional materials across a diverse array of applications. The ultimate goal is to prevent biofilm growth without exerting a biocidal effect on the cells, thereby reducing the spread of antimicrobial resistance.

2. Materials and methods

2.1. Chemistry

All starting reagents and solvents were purchased from commercial suppliers (Merck KGaA, Darmstadt, Germany; FluoroChem, Hadfield, UK) and used as received. Ludox HS-40 was used unmodified, while an amount was lyophilized before the use. Reactions involving air-sensitive reagents were carried out under a nitrogen atmosphere with anhydrous solvents, which were used without further drying. The obtained derivatives were characterized by FT-IR, Raman spectroscopy, XPS, and TGA analyses.

2.1.1. Nanoparticle functionalization

*2.1.1.1. GPTS derivatives **1s,l** and **2s,l**. Epoxy-functionalized nanoparticles (**5s**).* **General Procedure A.** A solution of GPTS (50 mg, 0.05 mL, 0.21 mmol) in dry ethanol (1.25 mL) was added dropwise to a suspension of the appropriate silica in dry ethanol (10 mL), under nitrogen atmosphere. The mixture was stirred at 60 °C for 16 h. The particles were recovered by centrifugation, washed five times with ethanol, and dried under vacuum at 50 °C for 4 h to afford the desired product. Starting silica: suspension of Ludox HS-40 (940 mg, 4 wt% in water). Aspect: white powder. Obtained amount: 901 mg. FT-IR (cm^{-1}): 474 and 798 (Si–*O*–Si, bending vib), 956 (Si–OH, vib), 1111 (Si–*O*–Si, *asym* str vib), 1643 (bending OH vib, absorbed water), 2873 and 2939 (CH_2 *asym* and *sym* vib), 3210 (OH, str vib). Raman (cm^{-1}): 461 (Si–*O*–Si, rocking), 798 (Si–*O*–Si, bending vib), 918–1058 (Si–OH, def vib; Si–*O*–Si, str vib), 1257 and 1298 (C–O, str epoxide ring), 1411, 1459 and 1479 (CH_2, def and wag vib), 2893 and 2920 (CH_2, str vib).

*Epoxy-functionalized nanoparticles (**5l**).* The nanoparticles were obtained according to General Procedure A. Starting silica: lyophilized Ludox HS-40 (400 mg). Aspect: white powder. Obtained amount: 382 mg. FT-IR (cm^{-1}): 474 and 798 (Si–*O*–Si, bending vib), 956 (Si–OH, vib), 1099 (Si–*O*–Si, *asym* str vib), 1643 (bending OH vib, absorbed water), 2885 and 2939 (CH_2, *asym* and *sym* vib), 3236 (OH, str vib). Raman (cm^{-1}): 461 (Si–*O*–Si, rocking), 798 (Si–*O*–Si, bending vib), 918–1058 (Si–OH, def vib; Si–*O*–Si, str vib), 1257 and 1298 (C–O, str epoxide ring), 1411, 1459 and 1479 (CH_2, def and wag vib), 2893 and 2920 (CH_2, str vib).

*Salicylic-functionalized nanoparticles (**1s**).* **General Procedure B.** The appropriate epoxy-functionalized silica nanoparticles (60 mg) were suspended in dry ethanol (1.5 mL), and a solution of the desired acid (0.20 mmol) in dry ethanol (2 mL) was added dropwise, under nitrogen atmosphere. The mixture was stirred at room temperature for 24 h. The particles were recovered by centrifugation, washed five times with ethanol, and dried under vacuum at 50 °C for 4 h to obtain the desired product. Starting reagents: epoxy-functionalized nanoparticles obtained from Ludox HS-40 suspension (**5s**) and *p*-aminosalicylic acid. Aspect: light brown powder. Obtained amount: 53 mg. FT-IR (cm^{-1}): 466 (Si–*O*–C, *asym* def vib), 798 (Si–*O*–C, *sym* str), 957 (Si–OH, str vib), 1096–1211 (Si–*O*–C, *asym* str; Si–*O*–Si, Si–OH, def vib), 1620 and 1654 (C═O, *sym* str vib), 2870–2978 (C–H, str vib), 3267 (N–H, str vib).

*Salicylic-functionalized nanoparticles (**1l**).* The nanoparticles were obtained according to General Procedure B. Starting reagents: epoxy-functionalized nanoparticles obtained from lyophilized Ludox HS-40 (**5l**), and *p*-aminosalicylic acid. Aspect: white powder. Obtained amount: 55 mg. FT-IR (cm^{-1}): 466 (Si–*O*–C, *asym* def vib), 798 (Si–*O*–C, *sym* str), 957 (Si–OH, str vib), 1096–1211 (Si–*O*–C, *asym* str; Si–*O*–Si, Si–OH, def vib), 1620 and 1654 (C═O, *sym* str vib), 2870–2978 (C–H, str vib), 3267 (N–H, str vib).

*Cinnamic-functionalized nanoparticles (**2s**)*. The nanoparticles were obtained according to General Procedure B. Starting reagents: epoxy-functionalized nanoparticles obtained from Ludox HS-40 suspension (**5s**), and *p*-aminocinnamic acid. Aspect: light yellow powder. Obtained amount: 47 mg. FT-IR (cm^{-1}): 478 (Si–*O*–C, *asym* def vib), 802 (Si–*O*–C, *sym* str), 956 (Si–OH, str vib), 1112–1200 (Si–*O*–C, *asym* str; Si–*O*–Si, Si–OH, def vib), 1612 and 1654 (C═O, *sym* str vib), 2873–2958 (C–H, str vib), 3310 (N–H, str vib). Raman (cm^{-1}): 442 (Si–*O*–Si, rocking), 797 (Si–*O*–Si, bending vib), 979 (Si–OH, str vib), 1060–1129 (Si–OH, def vib; Si–*O*–Si, str vib), 1410 and 1457 (CH_2, def and wag vib), 1599 and 1633 (-C═C-, str vib aromatic ring), 2893 and 2920 (CH, str vib).

*Cinnamic-functionalized nanoparticles (**2l**)*. The nanoparticles were obtained according to General Procedure B. Starting reagents: epoxy-functionalized nanoparticles obtained from lyophilized Ludox HS-40 (**5l**), and *p*-aminocinnamic acid. Aspect: white powder. Obtained amount: 53 mg. FT-IR (cm^{-1}): 478 (Si–*O*–C, *asym* def vib), 802 (Si–*O*–C, *sym* str), 956 (Si–OH, str vib), 1112–1200 (Si–*O*–C *asym* str; Si–*O*–Si, Si–OH, def vib), 1612 and 1654 (C═O, *sym* str vib), 2873–2958 (C–H, str vib), 3310 (N–H, str vib). Raman (cm^{-1}): 442 (Si–*O*–Si, rocking), 797 (Si–*O*–Si, bending vib), 979 (Si–OH, str vib), 1060–1129 (Si–OH, def vib; Si–*O*–Si, str vib), 1410 and 1457 (CH_2, def and wag vib), 1599 and 1633 (-C═C-, str vib aromatic ring), 2893 and 2920 (CH, str vib).

*2.1.1.2. APTES derivatives **3s,l** and **4s,l**. Amino-functionalized nanoparticles (**6s**)*. **General Procedure C.** A solution of APTES (125 mg, 0.132 mL, 0. 56 mmol) in 3 mL of dry ethanol was added dropwise to a suspension of the appropriate silica in 10 mL of dry ethanol, under nitrogen atmosphere. The mixture was stirred at 60 °C for 16 h. The particles were recovered by centrifugation, washed five times with ethanol, and dried under vacuum at 50 °C for 4 h to obtain the desired product. Starting silica: suspension of Ludox HS-40 (940 mg, 40 wt % in water). Aspect: white powder. Obtained amount: 877 mg. FT-IR (cm^{-1}): 462 (Si–*O*–C, *asym* def vib), 795 (Si–*O*–C, *sym* str), 956 (Si–OH, str vib), 1091 (Si–*O*–C, *asym* str; Si–*O*–Si, Si–OH, def vib), 1543 (N–H, def vib), 2873–2939 (C–H, str vib), 3209 (N–H and OH, str vib). Raman (cm^{-1}): 445 (Si–*O*–Si, rocking), 787 (Si–*O*–Si, bending vib), 979–1043 (Si–OH, def vib; Si–*O*–Si, str vib), 1318 (NH_2, rock vib), 1413 (CH_2, wag/twisting vib), 1453 (CH_2, def vib), 2897–2962 (CH, str vib), 3420 (NH, str vib).

*Amino-functionalized nanoparticles (**6l**)*. The nanoparticles were obtained according to General Procedure C. Starting silica: lyophilized Ludox HS-40 (1000 mg). Aspect: white powder. Obtained amount: 918 mg. FT-IR (cm^{-1}): 462 (Si–*O*–C, *asym* def vib), 795 (Si–*O*–C, *sym* str), 956 (Si–OH, str vib), 1091 (Si–*O*–C, *asym* str; Si–*O*–Si, Si–OH, def vib), 1543 (N–H, def vib), 2873–2939 (C–H, str vib), 3209 (N–H and OH, str vib). Raman (cm^{-1}): 445 (Si–*O*–Si, rocking), 787 (Si–*O*–Si, bending vib), 979–1043 (Si–OH, def vib; Si–*O*–Si, str vib), 1318 (NH_2, rock vib), 1413 (CH_2, wag/twisting vib), 1453 (CH_2, def vib), 2897–2962 (CH, str vib), 3420 (NH, str vib).

*Succinic-functionalized nanoparticles (**7s**)*. **General Procedure D.** Dry pyridine (0.06 mL) was added to a suspension of the appropriate amino-functionalized nanoparticles (250 mg) in dry dichloromethane (5 mL), under nitrogen atmosphere. Then, a solution of succinic anhydride (71 mg) in dry tetrahydrofuran (5 mL) was added dropwise to the suspension. The reaction mixture was stirred at room temperature for 24 h under nitrogen atmosphere. The particles were recovered by centrifugation, washed five times with ethanol, and dried under vacuum at 50 °C for 4 h to obtain the desired product. Starting reagent: amino-functionalized nanoparticles obtained from Ludox HS-40 suspension (**6s**). Aspect: white powder. Obtained amount: 233 mg. FT-IR (cm^{-1}): 474 (Si–*O*–C, *asym* def vib), 802 (Si–*O*–C, *sym* str), 956 (Si–OH, str vib), 1111 (Si–*O*–C, *asym* str; Si–*O*–Si, Si–OH, def vib), 1558 (N–H, def vib), 1701 (C═O, str vib), 2866–2939 (C–H, str vib), 3309 (N–H and OH, str vib). Raman (cm^{-1}): 441 (Si–*O*–Si, rocking), 665 (NH, def vib out of plane amide), 791 (Si–*O*–Si, bending vib), 954–1049 (Si–OH, def vib; Si–*O*–Si, str vib), 1275 (amide III band), 1313 (amide II band), 1418, and 1445 (CH_2, def and wag vib), 1556 (amide II band), 1718 (C═O, str amide), 1771 (C═O, str acid), 2896–2935 (CH, str vib), 3426 (NH, str vib).

*Succinic-functionalized nanoparticles (**7l**)*. The nanoparticles were obtained according to General Procedure D. Starting reagent: amino-functionalized nanoparticles obtained from lyophilized Ludox HS-40 (**6l**). Aspect: white powder. Obtained amount: 203 mg. FT-IR (cm^{-1}): 474 (Si–*O*–C, *asym* def vib), 802 (Si–*O*–C, *sym* str), 956 (Si–OH, str vib), 1111 (Si–*O*–C, *asym* str; Si–*O*–Si, Si–OH, def vib), 1558 (N–H, def vib), 1701 (C═O, str vib), 2866–2939 (C–H, str vib), 3309 (N–H and OH, str vib). Raman (cm^{-1}): 441 (Si–*O*–Si, rocking), 665 (NH, def vib out of plane amide), 791 (Si–*O*–Si, bending vib), 954–1049 (Si–OH, def vib; Si–*O*–Si, str vib), 1275 (amide III band), 1313 (amide II band), 1418, and 1445 (CH_2, def and wag vib), 1556 (amide II band), 1718 (C═O, str amide), 1771 (C═O, str acid), 2896–2935 (CH, str vib), 3426 (NH, str vib).

*Salicylic-functionalized nanoparticles (**3s**)*. **General Procedure E.** A solution of DCC (120 mg, 0.58 mmol) in dry dimethylformamide (0.5 mL) was added to a dispersion of the appropriate succinic-functionalized nanoparticles (40 mg) in dry dimethylformamide (0.5 mL), under nitrogen atmosphere. The mixture was stirred at room temperature for 20 min. Then, a solution of the desired acid derivative (0.30 mmol) in dry dimethylformamide (2 mL) was added dropwise, and the reaction was stirred at room temperature for 16 h. The particles were recovered by centrifugation, washed five times with ethanol, and dried under vacuum at 50 °C for 4 h to obtain the desired product. Starting reagents: succinic-functionalized nanoparticles obtained from Ludox HS-40 suspension (**7s**), and *p*-aminosalicylic acid. Aspect: light grey powder. Obtained amount: 29 mg. FT-IR (cm^{-1}): 478 (Si–*O*–C, *asym* def vib), 798 (Si–*O*–C, *sym* str), 960 (Si–OH, str vib), 1110 (Si–*O*–C, *asym* str; Si–*O*–Si, Si–OH, def vib), 1408 and 1438 (-C═C-, str vib aromatic), 1558 (amide band II), 1624 and 1654 (C═O, *sym* str vib), 2854–2931 (C–H, str vib), 3302 (N–H, str vib). Raman (cm^{-1}): 455 (Si–*O*–Si, rocking), 636 (NH, def vib out of plane amide), 801 (Si–*O*–Si, bending vib; –C═C–H, out of plane def vib), 970 (Si–OH, str vib), 1028–1068 (Si–OH, def vib; Si–*O*–Si, str vib), 1177 (-C═C–H, out of plane def vib), 1253 and 1300 (amide II band), 1411 and 1446 (CH_2, def and wag vib), 1533 (amide II band), 1606 and 1628 (-C═C-, str vib aromatic ring), 1682 (C═O, str vib amide), 2850–2935 (CH, str vib).

*Salicylic-functionalized nanoparticles (**3l**)*. The nanoparticles were obtained according to General Procedure E. Starting reagents: succinic-functionalized nanoparticles obtained from lyophilized Ludox HS-40 (**7l**), and *p*-aminosalicylic acid. Aspect: light-grey powder. Obtained amount: 34 mg. FT-IR (cm^{-1}): 478 (Si–*O*–C, *asym* def vib), 798 (Si–*O*–C, *sym* str), 960 (Si–OH, str vib), 1110 (Si–*O*–C, *asym* str; Si–*O*–Si, Si–OH, def vib), 1408 and 1438 (-C═C-, str vib aromatic), 1558 (amide band II), 1624 and 1654 (C═O, *sym* str vib), 2854–2931 (C–H, str vib), 3302 (N–H, str vib). Raman (cm^{-1}): 455 (Si–*O*–Si, rocking), 636 (NH, def vib out of plane amide), 801 (Si–*O*–Si, bending vib; –C═C–H, out of plane def vib), 970 (Si–OH, str vib), 1028–1068 (Si–OH, def vib; Si–*O*–Si, str vib), 1177 (-C═C–H, out of plane def vib), 1253 and 1300 (amide II band), 1411 and 1446 (CH_2, def and wag vib), 1533 (amide II band), 1606 and 1628 (-C═C-, str vib aromatic ring), 1682 (C═O, str vib amide), 2850–2935 (CH, str vib).

*Cinnamic-functionalized nanoparticles (**4s**)*. The nanoparticles were obtained according to General Procedure E. Starting reagents: succinic-functionalized nanoparticles obtained from Ludox HS-40 suspension (**7s**), and *p*-aminocinnamic acid. Aspect: light-yellow powder. Obtained amount: 33 mg. FT-IR (cm^{-1}): 474 (Si–*O*–C, *asym* def vib), 802 (Si–*O*–C, *sym* str), 956 (Si–OH, str vib), 1112 (Si–*O*–C, *asym* str; Si–*O*–Si, Si–OH, def vib), 1408 and 1438 (-C═C-, str vib), 1558 (amide band II), 1627 and 1651 (C═O, *sym* str vib), 1700 (C═O, str vib), 2862–2935 (C–H, str vib), 3318 (N–H, str vib), 3450 (O–H, str vib). Raman (cm^{-1}): 458 (Si–*O*–Si, rocking), 633 (NH, def vib out of plane amide), 801 (Si–*O*–Si, bending vib; –C═C–H, out of plane def vib), 970 (Si–OH, str vib), 1026–1046 (Si–OH, def vib; Si–*O*–Si, str vib), 1177 (-C═C–H, out of

plane def vib), 1255 (amide III band), 1312 (amide II band), 1411 and 1442 (CH_2, def and wag vib), 1532 (amide II band), 1609 and 1627 (-C═C-, str vib aromatic ring), 1689 (C═O, str vib amide), 2853–2932 (CH, str vib).

Cinnamic-functionalized nanoparticles ***(4l)***. The nanoparticles were obtained according to General Procedure E. Starting reagents: succinic-functionalized nanoparticles obtained from lyophilized Ludox HS-40 (**7l**), and *p*-aminocinnamic acid. Aspect: light-yellow powder. Obtained amount: 36 mg. FT-IR (cm^{-1}): 474 (Si–*O*–C, *asym* def vib), 802 (Si–*O*–C, *sym* str), 956 (Si–OH, str vib), 1112 (Si–*O*–C, *asym* str; Si–*O*–Si, Si–OH, def vib), 1408 and 1438 (-C═C-, str vib), 1558 (amide band II), 1627 and 1651 (C═O, *sym* str vib), 1700 (C═O, str vib), 2862–2935 (C–H, str vib), 3318 (N–H, str vib), 3450 (O–H, str vib). Raman (cm^{-1}): 458 (Si–*O*–Si, rocking), 633 (NH, def vib out of plane amide), 801 (Si–*O*–Si, bending vib; –C═C–H, out of plane def vib), 970 (Si–OH, str vib), 1026–1046 (Si–OH, def vib; Si–*O*–Si, str vib), 1177 (-C═C–H, out of plane def vib), 1255 (amide III band), 1312 (amide II band), 1411 and 1442 (CH_2, def and wag vib), 1532 (amide II band), 1609 and 1627 (-C═C-, str vib aromatic ring), 1689 (C═O, str vib amide), 2853–2932 (CH, str vib).

2.1.2. Functionalized nanoparticle characterization

2.1.2.1. Fourier-transform infrared spectroscopy (FT-IR). FT-IR spectra were acquired on a Shimadzu Prestige-21 FT-IR spectrophotometer (Shimadzu, Kyoto, Japan), equipped with a KBr attachment (Pike Technologies, Fitchburg, WI, USA). The analysis was carried out in the spectral range 450–4000 cm^{-1}, by collecting and averaging 50 scans for a final resolution of 8 cm^{-1}.

2.1.2.2. Raman spectroscopy. Raman spectra were acquired on a LabRAM HR Evolution (Horiba, Kyoto, Japan), using a 633 nm laser, 15 s acquisition time, 250 accumulations, hole: 100 with a 300 grating.

2.1.2.3. Thermogravimetric Analysis (TGA). Thermogravimetric Analysis (TGA) was performed to determine the degree of surface functionalization of the nanoparticles, using the following procedure. After surface modification, nanoparticle samples were dialyzed against DI water for 3 days to remove any unreacted groups from the dispersion, using cellulose dialysis tubing (Merck KGaA) with a MW cut-off ~ 14,000. Following dialysis, a sample of all nanoparticle dispersions was set aside for TGA analysis. First, dispersions were frozen in a freezer overnight (−4 °C) and then dried by freeze-drying using a Christ Alpha 2–4 LD plus system (Martin Christ Gefriertrocknungsanlagen GmbH, Osterode am Harz, Germany). TGA analysis was then undertaken using a Netzsh TG209 Thermal Analysis system (Erich Netzsh B.V. & Co. Holding KG, Selb, Germany). Dried nanoparticles were heated from room temperature to 800 °C at a heating rate of 10 °C/min under a nitrogen atmosphere. The mass of polymer bound to the particle surface was calculated from the weight loss measured between 150 and 800 °C. The mass retained at 800 °C after polymer decomposition was assumed to be the mass of the bare nanoparticles.

2.1.2.4. X-ray photoelectron spectroscopy (XPS). X-ray photoelectron spectra (XPS) were collected using a PHOIBOS 100 hemispherical analyzer (SPECS Surface Nano Analysis GmbH, Berlin, Germany). The X-ray excitation wavelength was provided by Al Kα radiation with a photon energy of 1486.6 eV. The XPS data were analyzed using CasaXPS software [24].

2.1.3. Preparation of the coated surfaces *A, B, C, and D*

Round glass coverslips (19 mm diameter, 0.5–0.6 mm thickness; Knittel G419-5 premium cover slips No. 5; Waldemar Knittel Glasbearbeitungs, Braunschweig, Germany) were cleaned with ethanol and incubated in 0.5 % poly(ethylenimine) (PEI) solution for 10 min at room temperature to form an adhesive layer on the glass surface. The PEI was thoroughly rinsed from the coverslip with deionized water and the surfaces dried under a stream of nitrogen gas. Ludox HS-40 and functionalized nanoparticle solutions were prepared as 4 wt% dispersions in deionized water for spin-coating. The glass coverslips were mounted directly onto the spin coater holder and 20 μL of the relevant nanoparticle dispersion was pipetted onto the coverslip surface, after which the coverslip was spun at 5000 rpm for 30 s. The coatings were cured for 1 h at 120 °C, and thereafter, thoroughly rinsed with deionized water and dried under a stream of nitrogen gas.

2.1.4. Coating characterization

2.1.4.1. Scanning electron microscopy (SEM). SEM measurements were performed on a JEOL SEM-EDS JSM IT500LV (JEOL Ltd., Tokyo, Japan). Before the analysis, the samples were sputtered with gold with an Edwards Scancoat Six Sputter Coater (Edwards Ltd, Burgess Hill, UK). The samples were then fixed with a carbon double-sided tape on an aluminum disc (10 cm diameter) and inserted in the SEM chamber. The SEM micrographs (in secondary electrons, SE) were carried out in high vacuum (HV) conditions, with an accelerating voltage of 20 kV, load current of 2.53 μA, and 40 μA of probe current.

2.1.4.2. Atomic force microscopy (AFM). The surface morphology of silica nanoparticle films was examined using an Asylum MFP-3D Origin Atomic Force Microscope (Oxford Instruments, Abingdon, UK) operating in AC mode with a AC160OTS-R3 cantilever (spring constant ~ 26 N/m). Image scans of 40 μm × 40 μm were acquired. Median thickness and roughness parameters including Ra, Rq, Rsk, and Rku were calculated by Gwyddion 2.65 software from at least three random images for each sample, according to the ISO 21920–2:2021 standard.

2.1.4.3. Thickness. Samples were checked for thickness using a magnetic micrometer, taking 30 measurements for each specimen (MiniTest FH7200 equipped with FH4 probe, ø sphere = 1.5 mm; ElektroPhysik Dr. Steingroever, Köln, Germany).

2.1.4.4. Contact angle. The contact angle was measured from images purposely selected from a video recording a distilled water drop falling on the surface of the specimens. These were positioned on a black background, and a camera was mounted in front of them (GoPro Hero Session, US-CA; distance 10 cm). After starting the video mode, a drop of distilled water (of about 5 μL in volume), created by using a Pasteur pipette, was allowed to fall from 1 cm above the sample onto its surface. From the resulting video, selected photographs were saved and analyzed by a specific software (ImageJ). The latter allowed the automatic measurement of the contact angle between a baseline, corresponding to the surface on which the drop was lying, and the tangent to the drop. By having the operator choose two different points for each line, the latter were drawn by the software [25,26].

2.2. Microbiology

2.2.1. P. aeruginosa strain and growth conditions

The bacterial model *P. aeruginosa PA01* tagged with green fluorescent protein (GFP) was used in the study [27]. The strain was stored at −80 °C in a freezer medium containing 2 % peptone and 20 % glycerol. The microorganisms were grown at 30 °C for 24 h in the Luria Bertani (LB) medium, and bacterial cells were washed three times in Phosphate Buffer Saline (PBS, Merck KGaA) before being used in the subsequent experiments.

2.2.2. Biofilm growth

Biofilms were grown on coverslips prepared with modified nanoparticle (**A**, **B**, **C**, and **D**) coatings. Controls were set up by growing

biofilm on both untreated coverslips (**NT**) and coverslips coated with unmodified Ludox HS-40 (**L**). Coverslips were sterilized by 20 min soaking in 20 % ethanol followed by two washing steps in distilled sterile water. Then, biofilms were grown on each coverslip using 24-well microtiter plates following a literature method [28], with some modifications. Briefly, each well was filled with 3.8 mL of LB medium containing 10^8 cells/mL of a washed overnight culture. Coverslips were placed on the top of the wells so that the medium completely touched only the coated side of the slide. Then, the microtiter plate was turned upside down to avoid the formation of any air bubbles on the functionalized surface and it was incubated at 37 °C to promote bacterial adhesion. The outside air pressure pushed the coverslip against the bottom of the well keeping the slide in place without falling. After 24 h of incubation, coverslips with adhered bacteria were moved to a new microtiter plate and planktonic non-adhered cells were recovered. The new 24-well microtiter was prepared by filling each well with 3.8 mL of sterile 20 % diluted LB medium. Then, slices were placed on top of the wells, the microtiter plate was turned upside down and incubated at 37 °C for a further 24 h to allow biofilm development and maturation. Once the biofilm was grown, coverslips were collected from the microtiter wells and transferred to 2 mL of PBS. Sessile cells were removed from the coated surfaces by gently pipetting and vortex mixing for 30 s and processed for analysis. Three biological replicates were performed for each coating surface.

2.2.3. Cell viability

Serial dilutions of the resulting biofilm or non-adhered cell suspensions were plated on LB agar and incubated overnight at 37 °C. Colony-forming units (CFUs) were determined by the standard colony counting method. Biofilm data were reported as the number of viable bacterial cells normalized to the area, and means were calculated. The efficacy of the anti-biofilm material was calculated as a percentage reduction of the CFUs to the controls. Five technical replicates were performed for each experiment.

2.2.4. Relative bacterial death rate

500 μL of each biofilm or non-adhered cell suspensions were incubated with the BacLight Red bacterial stain (final concentration: 0.2 μM; B-35001, Invitrogen, Waltham, MA, USA) according to the manufacturer's instructions. Biofilms were incubated for 15 min in the dark, at room temperature. 100 μL of stained suspensions were aliquoted on black-sided plates, and fluorescence intensity was measured using the Infinite 200 PRO Microplate Reader (Tecan, Männedorf, Switzerland) with excitation at 581 nm and emission at 644 nm. The relative death rate was determined by dividing the red fluorescent intensity by the number of viable cells obtained from the plate count assay; means were also calculated. Four technical replicates were performed for each experiment.

2.2.5. Cellular activity

Cellular activity within the biofilm was evaluated by measuring the GFP intensity of biofilm cells [29]. 100 μL of biofilm suspension was aliquoted on black-sided plates, and fluorescence intensity was measured using an Infinite 200 PRO Microplate Reader (Tecan), with excitation at 360 nm and emission at 465 nm. Fluorescent intensity data were normalized to the number of viable cells obtained from the plate count assay, and means were calculated. Four technical replicates were performed for each experiment.

2.2.6. Oxidative stress

500 μL of each biofilm suspension was incubated with the CellROX Green Reagent (final concentration 5 μM, C10444; Invitrogen) according to the manufacturer's instructions. Biofilms were incubated for 30 min at 37 °C in the dark. 100 μL of stained suspension was aliquoted on black-sided plates, and fluorescence intensity was measured using an Infinite 200 PRO Microplate Reader (Tecan), with excitation at 485 nm and emission at 535 nm. Fluorescent intensity data were normalized to the number of viable cells obtained from the plate count assay, and means were calculated. Four technical replicates were performed for each experiment.

2.2.7. Total proteins

200 μL of each biofilm suspension was broken by 30 s sonication at 30 % amplitude in a water bath, using a Branson 3510 instrument (Branson Ultrasonic Corporation, Danbury, CT, USA). Suspensions were centrifuged at 8000 g for 20 min, and the supernatant containing proteins was recovered. Proteins were quantified using a Qubit 4 fluorometer system (ThermoFisher Scientific, Waltham, MA, USA) and the Qubit protein assay kit (Q33211; ThermoFisher Scientific) according to the manufacturer's instructions. Micrograms of proteins were normalized to the number of viable cells obtained from the plate count assay, and means were calculated. Five technical replicates were performed for each experiment.

2.2.8. Statistical analysis

Any significant differences among the samples were evaluated by the two-tailed ANOVA analysis (GraphPad Prism Software, version 8.0.0, San Diego, California USA). The ANOVA analysis was carried out after verifying data independence (Pearson's Chi-square test), normal distribution (D'Agostino-Pearson normality test), and homogeneity of variances (Bartlett's test). Tukey's honestly significant difference test (HSD) was used for pairwise comparisons to determine the significance of the data. Statistically significant results were decided by p-values <0.05.

To evaluate the correlation among the parameters analyzed, a permutational multivariate analysis of variance (PERMANOVA) based on Bray-Curtis distance matrix was performed using the XLSTAT-R adonis function from the vegan package in R. Statistically significant results were decided by p-values <0.05.

The reduction/increase percentages of biofilm parameters in comparison to the controls were calculated as (coated surface data – control data) x 100/control data.

3. Results and discussion

3.1. Preparation of functionalized nanoparticles

Silica nanoparticles used in the coating of the glass coverslips were obtained from either a suspension (**s** series) or a lyophilisate (**l** series) of Ludox HS-40, functionalized with the appropriate acid derivative (*p*-aminosalicylic acid or *p*-aminocinnamic acid) by two different approaches. **1s,l-2s,l** (Scheme 1) were synthesized by the functionalization of the nanoparticles with (3-glycidyloxypropyl)trimethoxysilane (GPTS) [30], affording intermediates **5s,l**, which were then subjected to a nucleophilic substitution with the appropriate *p*-amino derivative. For the synthesis of **3s,l-4s,l** (Scheme 2), the nanoparticles were functionalized with (3-aminopropyl)triethoxysilane (APTES) [31], yielding intermediates **6s,l**, which underwent an acylation reaction with succinic anhydride to **7s,l**. The carboxylic function of these intermediates was then functionalized with the appropriate *p*-amino derivative to afford the desired nanoparticles **3s,l-4s,l**.

3.2. Nanoparticle characterization

3.2.1. Fourier-transform infrared spectroscopy (FT-IR)

Fourier Transform Infrared Spectroscopy (FT-IR) analyses of the GPTS (**1s,l** and **2s,l**) and APTES (**3s,l** and **4s,l**) functionalized silica nanoparticles are shown in Figs. 1 and 2, respectively (see also Table S1, Supporting Information).

GPTS series. The absorption bands characteristic of silica can be observed at ~474 and 798 cm^{-1} (asymmetric stretching vibrations, Si–*O*–Si), ~956 cm^{-1} (vibration bond, Si–OH), and ~1111 cm^{-1} (bending vibration, Si–*O*–Si). Peaks at ~1620 and ~1654 cm^{-1} in **1s,l**

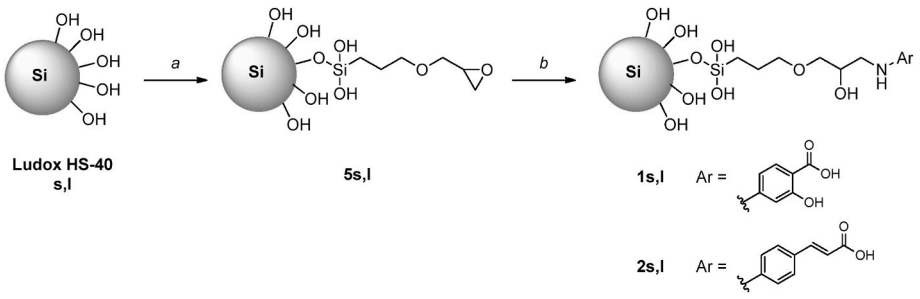

Scheme 1. Reagents and conditions: *a)* GPTS, dry ethanol, 60 °C, N_2 atm, 16 h; *b)* NH_2Ar, dry ethanol, RT, N_2 atm, 24 h.

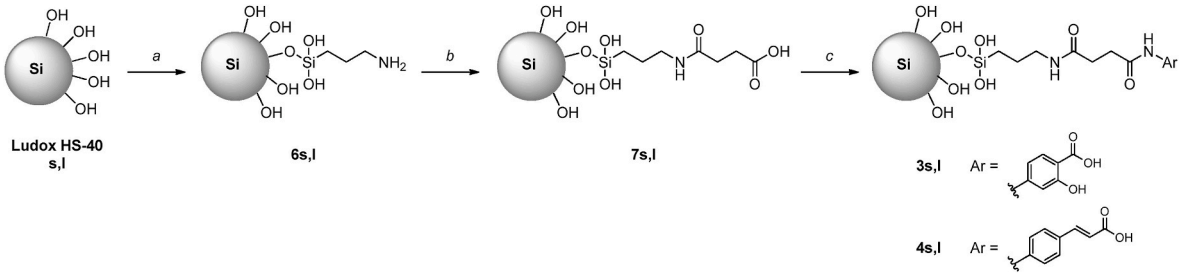

Scheme 2. Reagents and conditions: *a)* APTES, dry ethanol, 60 °C, N_2 atm, 16 h; *b)* succinic anhydride, dry DCM, dry pyridine, dry THF, RT, N_2 atm, 24 h; *c)* DCC, NH_2Ar, dry DMF, RT, N_2 atm, 16 h.

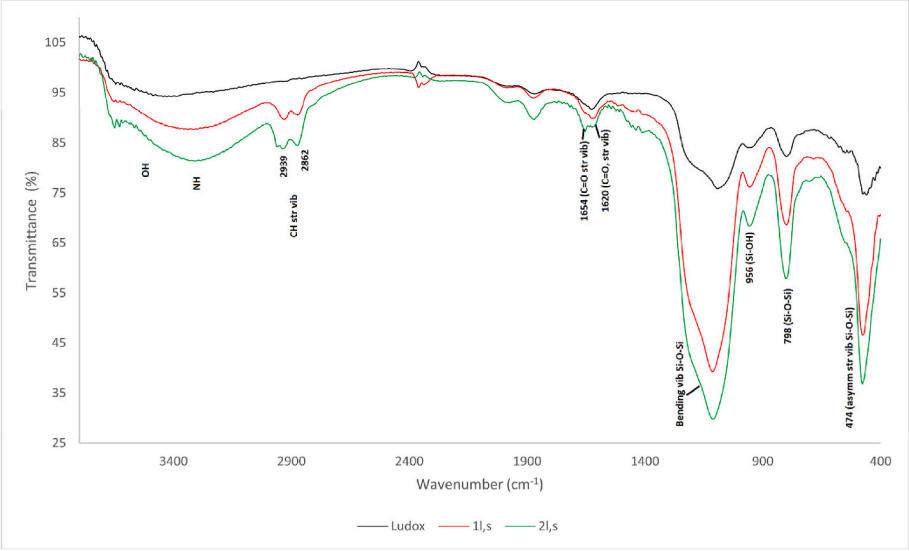

Fig. 1. FT-IR spectra of Ludox and GPTS derivatives **1s,l** and **2s,l**.

and **2s,l** can be attributed to the symmetric stretching vibration of C═O. CH stretching vibration at 2862 and 2939 cm^{-1}, OH stretching at around 3450 cm^{-1}, and N–H vibration at around 3310 cm^{-1} are also observed (Fig. 1, Table S1).

APTES series. The bands characteristic to silica are observed at around 474 (*asym* Si–*O*–C def vib), 798 (*sym* Si–*O*–C str), 956 (Si–OH str vib), 1111 cm^{-1} (bending vibration, Si–*O*–Si) and 3460 cm^{-1} (O–H stretching vibration), as previously assigned for the GPTS series. The band observed at 1639 cm^{-1} can be attributed to the bending vibration of the OH group of adsorbed water. The spectra exhibit bands characteristic of the functionalization of the silica nanoparticles: 1408 and ~1438 cm^{-1} (-C═C- stretching vibrations from the aromatic groups), 1558 cm^{-1} (NH bending vibration, amide II), ~1627 and 1654 cm^{-1} (C═O symmetric stretching vibration, amide, and aromatic carboxylic acid). The band at ~1700 cm^{-1}, observed in compound **4** but not in **3**, can be attributed to the symmetric stretching vibration of the carboxylic acid of the cinnamic derivative. CH stretching vibration at 2862 and 2939 cm^{-1}, OH stretching at around 3450 cm^{-1}, and N–H vibration at around 3310 cm^{-1} (as in **1** and **2**) are also observed (Fig. 2, Table S1).

3.2.2. *Raman spectroscopy*

The Raman analyses of the GPTS- and APTES-functionalized silica nanoparticles are reported in Figs. 3 and 4, respectively (Table S2). Unfortunately, the salicylic derivatives of the GPTS series (**1s,l**) could not be characterized by this technique due to their high fluorescence in the Raman spectra, despite the use of lasers at different wavelengths (633, 532, and 785 nm).

The typical bands for Ludox HS-40 are observed at ~442 cm^{-1} (rocking band of Si–*O*–Si), ~800 cm^{-1} (Si–*O*–Si bending vibration), ~977 cm^{-1} (Si–OH), and ~1013-1057 cm^{-1} (Si–OH def. vib. and

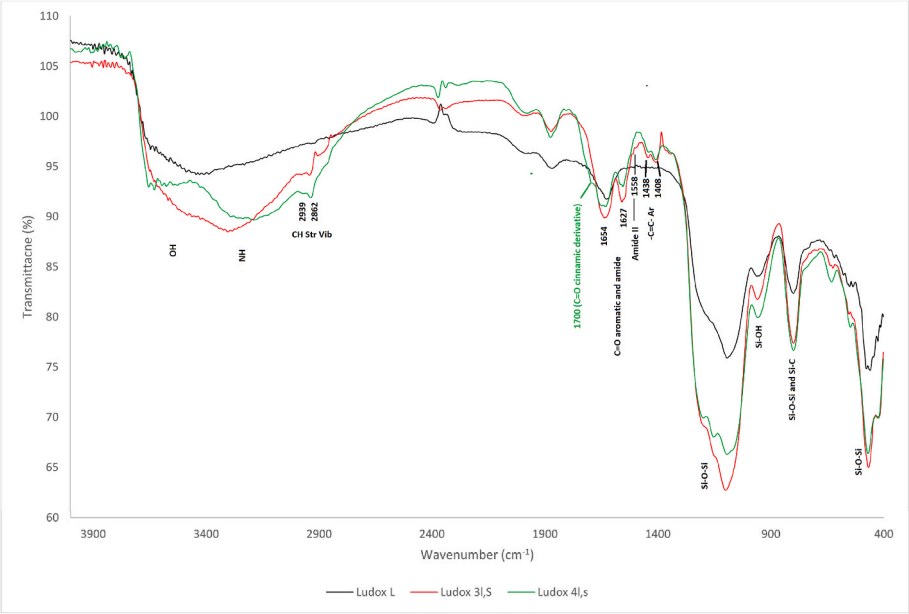

Fig. 2. FT-IR spectra of Ludox and APTES derivatives **3s,l** and **4s,l**.

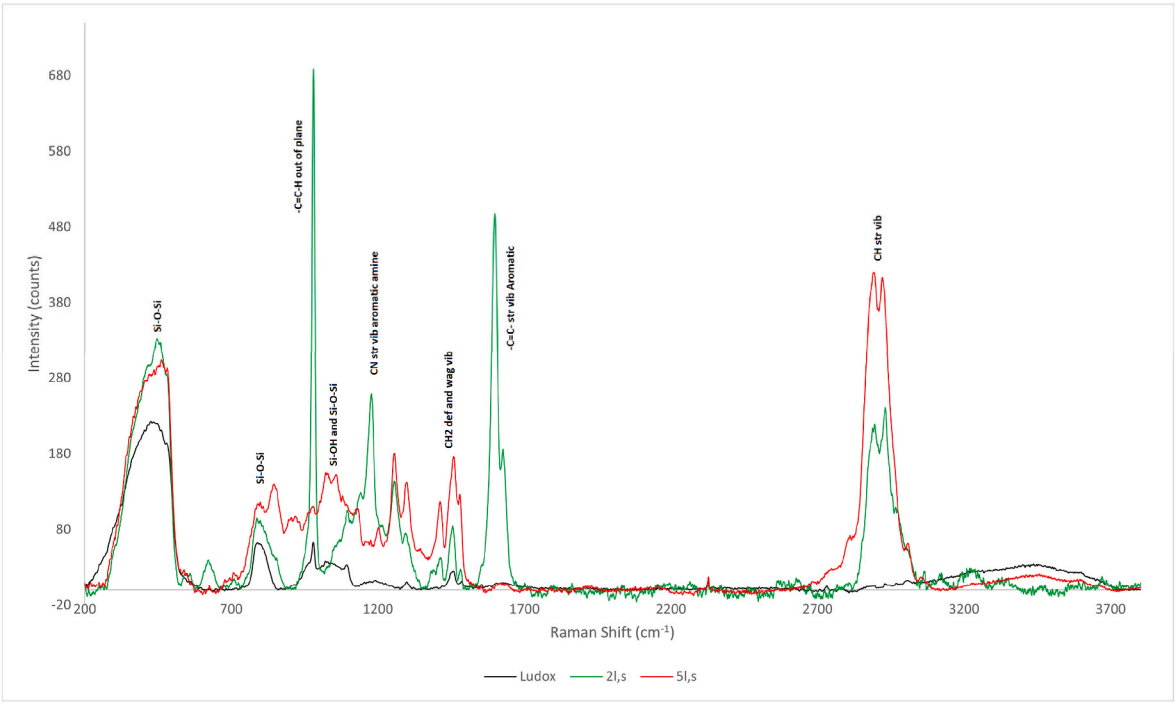

Fig. 3. Raman spectra of Ludox, final derivatives **2s,l**, and intermediates **5s,l**.

Si–*O*–Si str. vib.). The stretching vibration of O–H is also observed at around 3380 cm^{-1}.

GPTS series. The main characteristic bands for the derivatized silica nanoparticles **2s,l** are the aromatic bands at 1177 cm^{-1} (-C═C–H out of plane def. vib.), 1599 and 1633 cm^{-1} (-C═C- str. vib. of the aromatic ring), and 1255 cm^{-1} (C–N str aromatic amine), confirming the derivatization of the Ludox HS-40. Bands corresponding to the CH_2 groups are also observed at 1410 and 1457 cm^{-1} (CH_2 def. and wag. vib.) and around 2900 cm^{-1} (CH_2 str. vib.) (Fig. 3, Table S2).

APTES series. Similarly to the GPTS series, the main characteristic bands for the derivatized silica nanoparticles **3s,l** and **4s,l** are the aromatic bands at 801 cm^{-1} (-C═C–H out of plane def. vib., **3s,l**), 1177 cm^{-1} (-C═C–H in plane def. vib.), ~1600 and 1627 cm^{-1} (-C═C- str. vib. of the aromatic ring). Bands corresponding to the CH_2 groups are also observed at 1411 and ~1446 cm^{-1} (CH_2 def. and wag. vib.), and around 2900 cm^{-1} (CH_2 str. vib.). Amide II band (N–H def. vib.) and Amide III band (C–N str. vib.) are also observed at ~1312, ~1532, and ~1255 cm^{-1}, respectively (Fig. 4, Table S2).

3.2.3. *X-ray photoelectron spectroscopy (XPS) and Thermogravimetric Analysis (TGA)*

GPTS series. Both the suspension and the lyophilized samples demonstrated a similar increase in the relative nitrogen and carbon at the nanoparticles' surface, confirming functionalization with GPTS. The

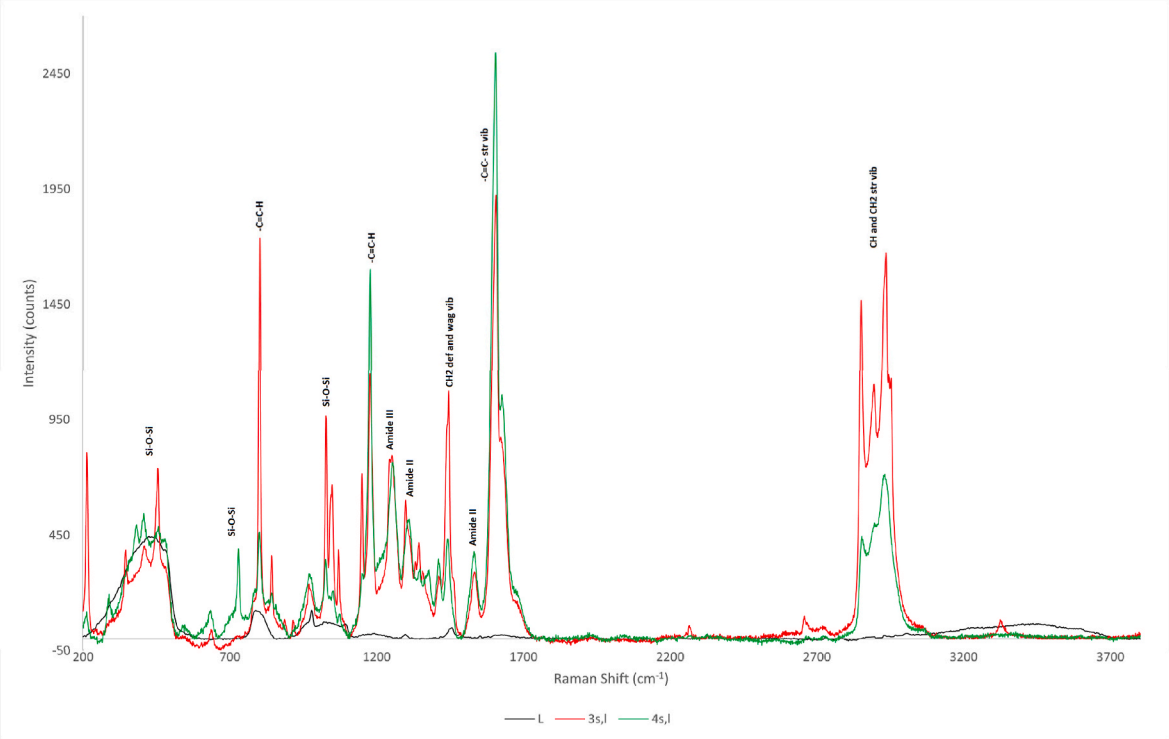

Fig. 4. Raman spectra of Ludox and final derivatives **3s,l** and **4s,l**.

addition of each functional derivative to the intermediate resulted in relatively minor changes in the overall elemental composition on the nanoparticles' surface. As for the suspension-derived nanoparticles, **2s** showed negligible changes in elemental composition relative to the **5s** intermediate, while the **1s** sample presented a small increase in carbon, and a minor reduction in nitrogen and oxygen. As for the lyophilized samples, the elemental composition of both **2l** and **1l** remained similar (Table 1). TGA analysis revealed that, for both functional derivatives, the degree of functionalization was greater on the lyophilized-modified nanoparticles compared to the suspension-modified nanoparticles (2.64 and 1.83 groups/nm^2 for **1l** and **2l**, and 0.74 and 0.87 groups/nm^2 for **1s** and **2s**, respectively) (Table 2).

APTES series. XPS analysis confirmed the addition of APTES to Ludox HS-40 (intermediate products **6s,l**) through an increase in nitrogen and carbon on the nanoparticle intermediates, relative to Ludox HS-40 as control (Table 1). After acylation with succinic anhydride and the functionalization of the carboxylic acid residue with the relevant *p*-amino derivative, the lyophilized samples (**4l**, **3l**) exhibited significant increases in nitrogen and carbon, relative to the intermediate (**7l**), indicating the successful covalent binding of the functional derivatives. For the suspension (**s**) samples, a lower increase in the relative nitrogen contribution to the surface chemistry indicated a lower level of derivatization relative to the lyophilized samples. This was confirmed by the TGA data, in which the density of functional groups per nm^2 on the particles was greater on the lyophilized samples (1.59 (**4l**) and 1.88 (**3l**) groups/nm^2 *vs* 0.96 (**4s**) and 1.05 (**3s**) groups/nm^2) (Table 2).

Table 1
XPS data revealing the elemental composition (Si, C, N, O) of the nanoparticles at different stages of modification.

Sample	Si	C	N	O
Ludox HS-40	32.52	7.32	0.32	59.84
1s	28.53	22.75	0.29	48.42
1l	29.61	21.97	0.41	47.54
2s	29.64	19.36	1	50.86
2l	28.69	23.32	0.37	47.19
3s	26.67	27.52	2.9	42.91
3l	8.55	69.45	7.12	14.89
4s	27.04	25.77	2.01	45.18
4l	7.78	70.28	7.34	14.6
5s	29.01	20.37	1	50.53
5l	30.06	19.06	1.13	49.78
6s	32.53	10.76	2.01	54.7
6l	27.35	26.19	1.05	45.4
7s	23.87	32.77	1.6	41.76
7l	31.33	15.67	1.03	51.97

Table 2
TGA data revealing the density of surface groups on the nanoparticles at different stages of the surface modification process.

Sample	M.W.	TGA value (groups/nm^2)
1s	*347.44*	0.74
1l		2.64
2s	*356.47*	0.87
2l		1.83
3s	*371.44*	1.05
3l		1.88
4s	*382.49*	0.96
4l		1.59
5s	*194.29*	1.24
5l		2.65
6s	*137.31*	1.31
6l		4.35
7s	*237.28*	1.31
7l		0.99

3.3. Coating preparation

Due to the higher degree of surface functionalization, the lyophilized samples **1l**–**4l** were used to coat round glass coverslips via spin-coating, affording **A**, **B**, **C,** and **D**, respectively. The outcome of the coating process was verified by SEM, AFM, and physical measurements. Finally, the anti-biofilm properties of the materials were analyzed.

3.4. Coating characterization

3.4.1. Atomic force microscopy (AFM)

Surface texture is an important factor in the understanding of the nature of material surfaces and plays an important role in their functional performance. Therefore, after preliminary SEM observations (Fig. S1), AFM topographic images were acquired to offer a detailed view and characterization of the coatings produced using unmodified

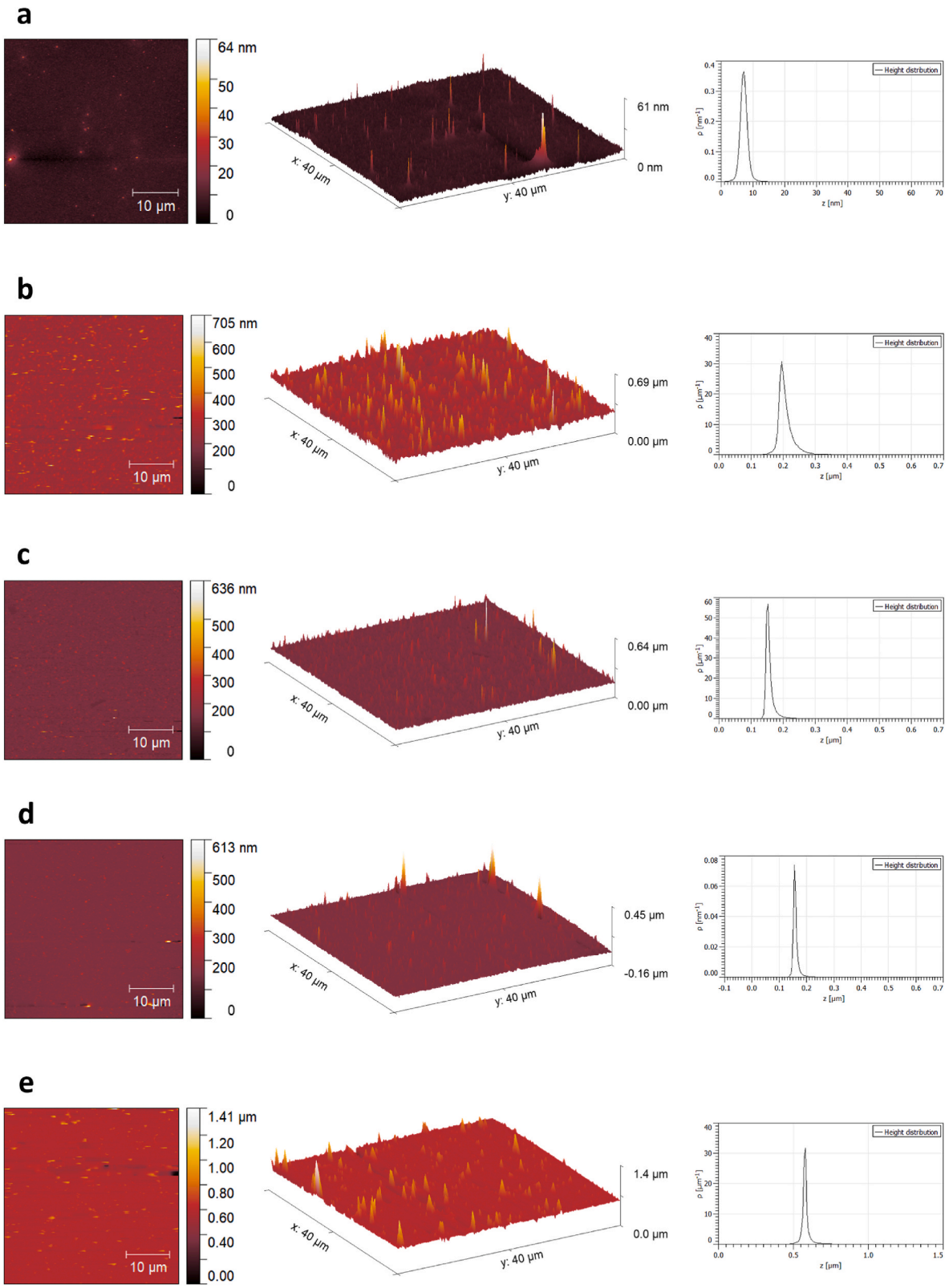

Fig. 5. Atomic force microscopy (AFM) topographic image (40 × 40 µm), 3D rendering of the 40 × 40 µm image for perspective, and surface height distributions of control **L** (**a**), **A** (**b**), **B** (**c**), **C** (**d**) and **D** (**e**).

Table 3
Median thickness and roughness parameters obtained from AFM image analysis of coatings prepared with Ludox HS-40 (**L**) and functionalized nanoparticles (**A**, **B**, **C**, and **D**).

Sample	Median thickness (nm)	Ra (nm)	Rq (nm)	Rsk	Rku
A	226.0 ± 22.7^{c}	21.5 ± 4.1^{c}	36.6 ± 9.7^{c}	2.2 ± 0.3^{b}	8.2 ± 1.7^{b}
B	141.6 ± 36.1^{b}	10.6 ± 2.3^{b}	18.6 ± 2.6^{b}	2.8 ± 0.6^{b}	14.0 ± 2.2^{ab}
C	135.3 ± 29.4^{b}	11.1 ± 3.8^{b}	19.2 ± 4.4^{b}	2.5 ± 0.5^{b}	12.2 ± 3.5^{ab}
D	647.5 ± 94.3^{d}	23.8 ± 7.1^{c}	35.9 ± 7.4^{c}	2.4 ± 0.5^{b}	16.3 ± 6.1^{a}
L	10.8 ± 2.4^{a}	1.8 ± 0.6^{a}	3.8 ± 0.4^{a}	1.7 ± 0.1^{a}	10.3 ± 1.7^{ab}

Data are expressed as the mean ± standard deviation of at least three images. Different superscript letters indicate significant differences (Tukey's HSD, $p \leq 0.05$) between the means of different coatings.

Ludox HS-40 (**L**) and the modified nanoparticles (**A**, **B**, **C**, and **D**) (Fig. 5).

AFM images of the modified nanoparticles revealed that materials functionalized with APTES presented a more heterogeneous coating, demonstrated by frequent, large agglomerations extending up to 100 nm from the surface (Fig. 5d and e). Conversely, the GTPS-derivatized samples showed a more confluent coating, improving the overall degree of surface coverage relative to the APTES series (Fig. 5b and c).

The median thickness was quantified from the AFM images and data are reported in Table 3. All the surfaces coated with modified particles displayed median thickness values statistically higher than the unmodified particles. Coatings **B** and **C** were statistically comparable, whereas **A** and **D** demonstrated higher values, with **D** significantly surpassing **A** in magnitude. PERMANOVA analysis confirmed that the variance of the median thickness was explained for 71.2 % by the modification of Ludox HS-40 ($p = 0.001$) and for 14.4 % by the combination between the type of both the linkers and the derivatives used in the functionalization procedure ($p = 0.001$).

To study the roughness of the coatings, AFM images were analyzed according to the ISO 21920–2:2021 standard (Table 3). Roughness average (Ra) provided a global evaluation of the roughness amplitude, whereas Root-mean-square roughness (Rq) was evaluated for its sensitivity to peaks and valleys, due to the squaring of the amplitude in its calculation [32]. Both parameters were quantified by the deviation of the profile of all the points from an ideal flat form. The increase in these values is correlated with the increase in the materials' roughness [32]. Our data indicated that all coatings with modified nanoparticles statistically increased the surface roughness compared to the unmodified Ludox HS-40. In detail, the Ra and Rq values were significantly higher in surfaces **A** and **D** relative to surfaces **B** and **C**.

While Ra and Rq provided a global evaluation of the roughness amplitude, they did not give information on the spatial frequency of the irregularities or the shape along the roughness profile [33]. Therefore, Skewness (Rsk) and Kurtosis (Rku) parameters were calculated to study the asymmetry and the sharpness of the height distribution, respectively. All coated surfaces displayed positive Rsk values, corresponding to high peaks on a flat, regular surface [33]. **L** showed values statistically lower than coatings with modified Ludox HS-40, suggesting a more symmetric distribution of peaks. Except for **A** and **D**, Rku values did not show statistical differences. All coatings presented Rku values above 3, indicating the predominance of sharp peaks with respect to flat peaks [33].

In summary, materials coated with modified Ludox HS-40 (**A**, **B**, **C**, and **D**) displayed a higher roughness with a lower symmetric distribution of sharp peaks in comparison to the materials coated with unmodified particles. In detail, the roughness of surfaces **A** and **D** was higher than that of surfaces **B** and **C**. PERMANOVA analysis confirmed that 65.1 % of the variability of all the analyzed parameters was explained by the modification of Ludox HS-40 ($p = 0.001$), and 20.8 % by the combination of both the type of linker and the derivatives added to the particles ($p = 0.001$).

3.4.2. Thickness

The measurements of the relative thickness of the glass coverslips (Table 4, Table S3) indicated a significantly increased thickness for the **A**, **C**, and **D** coatings obtained with the functionalized nanoparticles with respect to the sample produced with the Ludox HS-40 (**L**). In detail, samples **A** and **D** showed the highest thickness values, confirming the results obtained from the AFM analysis (Table 3).

Table 4
Thickness and contact angle values of coatings obtained with Ludox HS-40 (**L**) and functionalized nanoparticles (**A**, **B**, **C**, and **D**).

Sample	Thickness (μm) Average[a] ± s.d. (CV %)	Contact angle (°) Average[b] ± s.d. (CV %)
A	552.83 ± 1.76 (0.32)^{c}	61.86 ± 1.22 (1.97)^{a}
B	550.30 ± 1.88 (0.34)^{ab}	60.44 ± 1.55 (2.56)^{a}
C	551.43 ± 1.52 (0.28)^{b}	60.40 ± 1.35 (2.23)^{a}
D	554.60 ± 1.71 (0.31)^{d}	61.13 ± 1.98 (3.24)^{a}
L	550.20 ± 1.40 (0.25)^{a}	37.86 ± 1.00 (2.63)^{b}

Data are expressed as the mean ± SD of at least triplicate determinations. Different superscript letters indicate significant differences (Tukey's HSD, $p \leq 0.05$) between the means of different coatings.
[a] Mean of 30 measurements.
[b] Mean of 3 measurements.

3.4.3. Contact angle

Water contact angles of the nanoparticle-coated glass coverslips were measured by analyzing camera-acquired images (contact angle of the unfunctionalized sample: $49.86° \pm 7.16°$; CV % = 14.36). All data are presented in Table 4 and Fig. S2 (Supporting Information). Compared to Ludox HS-40 (**L**), the coating with the functionalized nanoparticles (**A**, **B**, **C**, and **D**) resulted in an increase in lipophilicity. Specifically, samples **A** and **D** were characterized by the highest contact angle values (see also Table S4 for more details).

3.5. Anti-biofilm activity of the coated surfaces

3.5.1. Anti-biofilm performance by plate count viability assay

The plate count viability assay was performed on both test (**A**, **B**, **C**, and **D**) and control surfaces (untreated and coated with unmodified Ludox HS-40, named **NT** and **L**, respectively) to determine the number of cells within the biofilm.

The data revealed that all coated surfaces displayed a significant reduction in biofilm formation compared to the **NT** control surface, with a percentage decrease ranging from -59.2 ± 2.2 (**B**) to -83.7 ± 3.4 (**D**) (Fig. 6, panel I). However, when the coated surfaces were compared to the **L** control, a reduction in biofilm formation was detected only for surfaces **A** and **D**, with a decrease of -42.6 ± 10.6 % and -54.0 ± 9.7 %, respectively (Fig. 6, panel I). Conversely, **B** and **C** displayed cell numbers statistically comparable to that of the control **L**. These results indicated that Ludox HS-40 particles alone can affect biofilm formation. Indeed, a comparison between **L** and **NT** revealed that Ludox HS-40 particles alone decreased biofilm formation by up to -64.5 ± 7.3 %. Accordingly, silica nanoparticles used as carriers for drug delivery have been previously proven to possess anti-biofilm properties due to their ability to promote the production of reactive oxygen species (ROS) [16].

Previous studies conducted by our research team have demonstrated that the activity of *p*-aminocinnamic acid relies on the presence of the

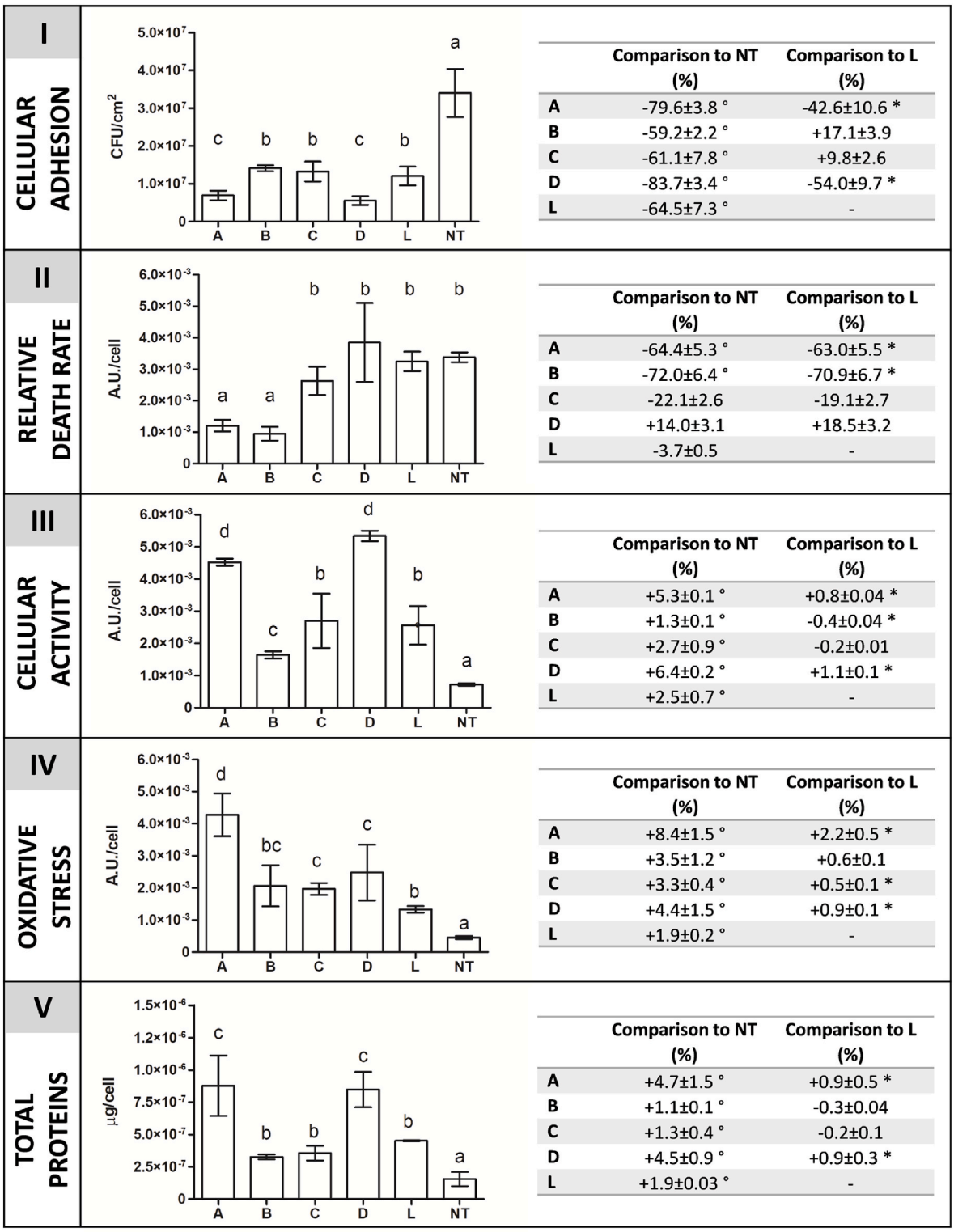

	Comparison to NT (%)	Comparison to L (%)
A	-79.6±3.8 °	-42.6±10.6 *
B	-59.2±2.2 °	+17.1±3.9
C	-61.1±7.8 °	+9.8±2.6
D	-83.7±3.4 °	-54.0±9.7 *
L	-64.5±7.3 °	-

	Comparison to NT (%)	Comparison to L (%)
A	-64.4±5.3 °	-63.0±5.5 *
B	-72.0±6.4 °	-70.9±6.7 *
C	-22.1±2.6	-19.1±2.7
D	+14.0±3.1	+18.5±3.2
L	-3.7±0.5	-

	Comparison to NT (%)	Comparison to L (%)
A	+5.3±0.1 °	+0.8±0.04 *
B	+1.3±0.1 °	-0.4±0.04 *
C	+2.7±0.9 °	-0.2±0.01
D	+6.4±0.2 °	+1.1±0.1 *
L	+2.5±0.7 °	-

	Comparison to NT (%)	Comparison to L (%)
A	+8.4±1.5 °	+2.2±0.5 *
B	+3.5±1.2 °	+0.6±0.1
C	+3.3±0.4 °	+0.5±0.1 *
D	+4.4±1.5 °	+0.9±0.1 *
L	+1.9±0.2 °	-

	Comparison to NT (%)	Comparison to L (%)
A	+4.7±1.5 °	+0.9±0.5 *
B	+1.1±0.1 °	-0.3±0.04
C	+1.3±0.4 °	-0.2±0.1
D	+4.5±0.9 °	+0.9±0.3 *
L	+1.9±0.03 °	-

Fig. 6. Anti-biofilm efficacy and responses to the presence of nanoparticles in control (**NT** and **L**) and functionalized surfaces (**A**, **B**, **C**, **D**). Panel I reports the number of adhered cells on the sample surfaces; Panel II shows the relative death rate of cells in the biofilm grown on the surfaces; Panel III displays the biofilm cellular activity by measurements of GFP intensity; Panel IV reports the biofilm oxidative stress; Panel V indicates the total number of proteins in the collected biofilms. In each panel, the table on the right shows the percentage of reduction/increase of data in comparison to both **NT** and **L** control surfaces. The mean ± standard deviation of at least three independent values is reported. Different letters indicate significant differences (Tukey's HSD, $p \leq 0.05$) between the means of different coatings. A circle (°) indicates significant differences (Tukey's HSD, $p \leq 0.05$) in comparison to the **NT** control surface, whereas a star (*) indicates significant differences (Tukey's HSD, $p \leq 0.05$) in comparison to the **L** control surface.

conjugated aromatic system and the carboxylate anion, which contributes to its hydrogen-donating ability [22]. Hence, when functionalizing particles, it is crucial to ensure that the active portion of the molecules faces outwards. This guarantees direct interaction of the functional moiety with bacterial targets, eliminating steric impediments, even during the early stage of biofilm formation. Binding *p*-aminosalicylic acid or *p*-aminocinnamic acid to a surface by exploiting the *para*-side of the aromatic ring has been proven to be an effective strategy to maintain their anti-biofilm activity [9]. Accordingly, both the GPTS and APTES linkers were bound to the amino group at the *para* position of the phenyl rings of the two molecules. PERMANOVA analysis revealed that 82.8 % of the variance in the anti-biofilm activity could be explained by the combination of the linker and the type of derivatives ($p = 0.002$). This analysis also showed no correlation between the antibiofilm activity and type of linker or derivative alone, highlighting that *i)* both *p*-aminosalicylic acid and *p*-aminocinnamic acid enhanced the intrinsic anti-biofilm activity of Ludox HS-40, and *ii)* both GPTS and APTES were suitable linkers for providing effective anti-biofilm performance.

In summary, **A** and **D**, characterized by the two different linkers bearing the two natural derivatives, showed the best anti-biofilm effects. Their activities were significantly improved compared to the surface coated with unfunctionalized silica nanoparticles (**L**), indicating a synergistic effect between the particles and the anti-biofilm molecules. On the contrary, **B** and **C** displayed lower anti-biofilm performances.

The AFM images evidenced that, although the APTES-functionalized nanoparticles had a heterogeneous coating, **D** presented a higher number of large agglomerates compared to **C**, as indicated by the thickness values. The presence of this large amount of functionalized material could be related to the better anti-biofilm activity of **D**. Regarding the GTPS series, both materials showed a more uniform coating. However, while **B** was characterized by small peaks and some bare areas, **A** presented more confluent peaks with small to medium dimensions. Again, the observations from the AFM images align with the thickness data and may be related to the better activity observed for **A**. Accordingly, PERMANOVA analysis showed that differences among the anti-biofilm performances of **A**, **B**, **C**, and **D** were explained for 62.6 % by the median thickness ($p = 0.001$), for 21.5 % by the surface roughness (Ra) ($p = 0.001$), and for 3.5 % by their combination ($p = 0.025$). Indeed, the better anti-biofilm activity of **A** and **D** was statistically correlated with their higher thickness and roughness compared to **B** and **C**. Surface properties, including roughness, are considered important factors governing bacterial adhesion to surfaces [34]. In a study by Singh et al. [35], Rq roughness values above 25 nm led to a significant decrease in bacterial adhesion and biofilm formation. It has been reported that nano-rough surfaces can restrain bacterial adhesion by decreasing the contact area between the bacteria and the surface [36]. Moreover, in our study, the increase in roughness likely provides a greater exposed surface, thereby resulting in an enhanced quantity of anti-biofilm molecules per unit area.

3.5.2. Relative bacterial death rate

The ability of both functionalized (**A**, **B**, **C**, and **D**) and control surfaces (**NT**, **L**) to kill both planktonic and sessile bacterial cells was tested to evaluate possible bactericidal effects. The results related to sessile cells (Fig. 6, panel II) revealed that **C** and **D** did not display significant differences compared to the **NT** and **L** control surfaces. In contrast, **A** and **B** showed a significantly lower relative death rate than both control samples. The death rates of planktonic cells (Table S5) in the bulk liquid of surfaces **B**, **C**, and **D** did not display significant differences in comparison to **NT**, whereas the relative death rate of cells in the planktonic bulk of surface **A** was even lower than both control samples. Accordingly, when non-adhered cells were plated for the viability assay, the number of CFU/mL was similar (**B**, **C** and **D**) or higher (**A**) in comparison to both controls (Table S6).These results suggest that the coated surfaces exerted their anti-biofilm activity with a mechanism that did not affect cell viability. Additionally, a comparison between **NT** and **L** control surfaces (in both planktonic and sessile cells) did not show statistical differences, indicating that the anti-biofilm contribution of the Ludox HS-40 particles alone was not due to a biocidal mechanism either. The development of a system able to inhibit biofilm formation through a non-toxic mechanism is a relevant step forward in fighting biofilm formation, as this approach prevents the emergence of anti-microbial resistance. Moreover, these results address the need for new products free of toxicological concerns, especially given the FDA's growing apprehensions about the toxic potential of nanoproducts and the wide range of potential applications of these nanosystems.

3.5.3. Cellular activity

The cell activity of sessile cells was studied by monitoring GFP fluorescence. This parameter can be considered a marker of cellular activity because, when constitutively expressed in cells, it is correlated with the rate of rRNA synthesis [29,37]. As shown in Fig. 6 (panel III), all coated surfaces and the **L** control surface displayed a significant increase in cellular activity compared to the **NT** control surface, with increases ranging from $+1.3 \pm 0.1$ (**B**) to $+6.4 \pm 0.2$ (**D**) folds. When comparing the coated surfaces to the **L** control surface, a statistical increase in cellular activity was observed only for the **A** ($+0.8 \pm 0.04$ folds) and **D** ($+1.1 \pm 0.1$ folds) samples, whereas a decrease was observed for **B** (-0.4 ± 0.04 folds). In addition, biofilm cells on the surface coated with Ludox HS-40 particles (**L**) were more active by $+2.5 \pm 0.7$ folds compared to the untreated surface (**NT**). These results indicate that Ludox HS-40 nanoparticles alone contributed to increasing cellular activity, with an enhanced effect when functionalized through the APTES and GPTS linkers with *p*-aminosalicylic acid (**D**) and *p*-aminocinnamic acid (**A**), respectively. Consistent with our results, silica systems have been reported to impact the metabolism of *E. coli*, leading to faster cellular growth and an associated alteration in nutritional capabilities [38].

Overall, our data indicate that the functionalized coated surfaces possess anti-biofilm properties without detrimental effects on bacterial cells. Thus, both *p*-aminosalicylic and *p*-aminocinnamic acids functionalized on silica nanoparticles retain their biocide-free anti-biofilm efficacy, as previously reported [11,12,22,23].

3.5.4. Oxidative stress

Many natural-based compounds exert their antibiofilm activity at sub-lethal concentrations by modulating the threshold level of ROS [39]. For instance, phenolic compounds with anti-biofilm activity can serve as pro-oxidants, perturbing the healthy redox cycle of cells and causing ROS accumulation [39] While a balanced redox cycle promotes microbial attachment and biofilm formation [40] sub-optimal ROS levels can discourage cell adhesion without killing cells [6]. Thus, the cellular response to ROS varies with the level of exposure: high levels lead to cell death, while lower levels can either promote or inhibit biofilm formation in a concentration-dependent manner.

This research investigated the oxidative stress within biofilm grown on coated surfaces. Data reported in Fig. 6 (panel IV) showed that all coated surfaces induced a significant increase in biofilm oxidative stress compared to the **NT** control surface, ranging from $+3.3 \pm 0.4$ (**C**) to $+8.4 \pm 1.5$ (**A**) folds. When comparing data from the coated surfaces to those of the **L** control surface, a statistical increase in ROS was also observed (ranging from $+0.5 \pm 0.1$ to $+2.2 \pm 0.5$ folds). Interestingly, the coated surfaces showing the most effective anti-biofilm performances, namely **A** and **D**, also displayed the highest ROS increase in biofilms. The biofilm on the **L** surface (control) also showed a 1.9 ± 0.2-fold increase in ROS production compared to the biofilm grown on the **NT** surface. This suggests that the increase of ROS within biofilms on the coated surface was partially attributable to Ludox HS-40. Accordingly, it has been reported that commercial silica colloidal particles, such as Ludox HS-40, provide suboptimal growth conditions that induce ROS production in *E. coli* K-12 cells [38]. This finding indicates that an increase in intracellular H_2O_2 mediates the redox response.

Several anti-biofilm compounds, including salicylic acid and cinnamic acid, function at sub-lethal concentrations through a ROS-mediated mechanism that involves the inhibition of WrbA enzymatic activity [11,22,23]. WrbA is a NADH:quinone oxidoreductase that prevents the accumulation of ROS by maintaining quinones in a fully reduced state. The lack of WrbA in an *E. coli* mutant strain did not impair the planktonic growth of the bacterium but significantly affected biofilm formation [11]. The loss of WrbA function led to a ROS-sensitive phenotype with a reduced capacity to develop biofilms. Accordingly, biofilm treated with salicylic acid was more prone to accumulate ROS than the control samples [23]. ROS are well-established signaling molecules and effectors in biofilms that can promote or reduce biofilm development according to the different levels of oxidative stress experienced by the cells [41–46]. In addition, it is widely acknowledged that ROS are involved in the maintenance of physiological functions, including the regulation of cellular activity [46]. This could also explain the observed increase in cellular activity within biofilms grown on coated surfaces (Fig. 6, panel III).

3.5.5. Total proteins

Proteins are key molecules in living cells, reflecting gene activity and cell viability. Quantitative measurement of proteins offers a snapshot of the balance between proteins' synthetic and degradative pathways, determining the global physiological state of cells [47]. In this research, proteins were extracted from biofilms grown on functionalized and control surfaces and subsequently quantified for comparison. Data normalized for the number of cells are reported in Fig. 6 (panel V). All funtionalized surfaces and the **L** control surface displayed a significant increase in total protein content compared to the **NT** sample, with an increase ranging from +1.1 ± 0.1 (**B**) to +4.7 ± 1.5 (**A**) folds. When comparing data from the functionalized surfaces to those of the **L** control surface, a statistically significant increase in total protein amount was observed only for **A** (+0.9 ± 0.5 folds) and **D** (+0.9 ± 0.3 folds). In addition, biofilms grown on surfaces coated with Ludox HS-40 particles (**L**) displayed a 1.9 ± 0.03-fold increase in proteins compared to the untreated surface (**NT**). Thus, the most effective anti-biofilm surfaces, **A** and **D**, displayed the highest increase in total protein content. These surfaces also generated greater levels of oxidative stress than the control samples, as shown in Fig. 6 (panel IV). Our findings are consistent with previous investigations where *Candida albicans* biofilms treated with non-lethal concentrations of zosteric acid—sharing the same scaffold as *p*-aminocinnamic acid and acting through a ROS-mediated mechanism—showed increased total protein content compared to the control [48].

Therefore, both the modified and unmodified Ludox HS-40 particles coated onto the surface did not harm the attached cells, which maintained a healthy protein synthesis machinery. The highest total protein content observed in **A** and **D** surfaces likely reflects cell adaptation to changing environments and mild stress conditions, as reported by several authors [49–51]. Sublethal concentrations of *p*-aminosalicylic and *p*-aminocinnamic acids showcase remarkable anti-biofilm activity by serving as pro-oxidants. This effect perturbs redox homeostasis and causes an accumulation of ROS [39]. As a result, the number of attached cells decreases, while cells enhance protein synthesis to cope with the perceived oxidative stress [39,52].

4. Conclusions

The proposed functionalization of silica nanoparticles with natural compound derivatives proved to be highly effective, especially when using lyophilized starting materials (series **l**), as confirmed by XPS and TGA analyses. The obtained derivatives (**1l**–**4l**) were then used to coat glass surfaces, and their anti-biofilm activity against *P. aeruginosa* was assessed. The coated surfaces **A** and **D**, characterized by the greatest thickness and roughness values, exhibited interesting anti-biofilm properties without affecting microbial viability. This reduction in microbial pressure helps mitigate the development of drug-resistant mutations. Interactions with the new surfaces triggered different microbial responses, including increased cellular activity, total protein amount, and oxidative stress levels. Conversely, **B** and **C** were less effective in inhibiting biofilm formation. Interestingly, the statistical analysis revealed no correlation between the antibiofilm activity and the specific linker or derivative alone. This observation highlights the potential of both the natural compound derivatives and linkers in creating innovative materials with good anti-biofilm performances. The better anti-biofilm activity of materials **A** and **D** was primarily attributed to the physical properties of the surface, particularly the higher thickness, and roughness compared to **B** and **C**. Indeed, SEM and AFM images of the surfaces revealed that the homogeneity of the coatings needs to be improved. Therefore, further studies will focus on optimizing the coating processes (*i.e.*, spray coating), to improve the quality of the obtained surfaces. Additionally, the incorporation of the particles into different materials, such as thermoplastics, will be explored.

Overall, the newly functionalized nanoparticles hold significant promise as alternative, biocide-free strategies for preventing or modulating biofilm formation. Considering their versatility, these functionalized nanoparticles can be tailored for a wide range of applications and incorporated into various materials to create effective antibiofilm interfaces. This approach has the potential to be highly beneficial in both clinical and industrial settings, particularly where biofilm formation by multi-drug resistant bacteria poses a critical challenge.

CRediT authorship contribution statement

Giulia Cazzaniga: Formal analysis, Investigation, Methodology, Validation, Writing – original draft, Writing – review & editing. **Cristina Cattò:** Formal analysis, Investigation, Methodology, Validation, Writing – original draft, Writing – review & editing. **Matteo Mori:** Formal analysis, Investigation, Writing – original draft, Writing – review & editing. **Patricia Hayes:** Formal analysis, Investigation, Writing – original draft, Writing – review & editing. **Dan Yang:** Investigation. **Nuwan H. Arachchi:** Investigation. **Federica Villa:** Resources, Supervision, Writing – review & editing. **Francesca Cappitelli:** Resources, Supervision, Writing – review & editing. **Alice Melocchi:** Formal analysis, Investigation, Methodology, Writing – original draft, Writing – review & editing. **Lucia Zema:** Resources, Supervision, Writing – review & editing. **Stefania Crespi:** Investigation. **Paul J. Molino:** Formal analysis, Investigation, Methodology, Resources, Validation, Writing – original draft, Writing – review & editing. **Stefania Villa:** Conceptualization, Supervision, Writing – review & editing, Resources. **Arianna Gelain:** Conceptualization, Resources, Writing – original draft, Writing – review & editing.

Data availability statement

The raw/processed data required to reproduce these findings cannot be shared at this time as the data also forms part of an ongoing study.

Declaration of competing interest

The authors declare that they have no known competing financial interests or personal relationships that could have appeared to influence the work reported in this paper.

Acknowledgments

The authors thank the Australian National Fabrication Facility (ANFF) – Materials Node for the use of facilities.

An unedited version of this paper containing preliminary results has been shared as a preprint on SSRN (https://doi.org/10.2139/ssrn.4823351).

Appendix A. Supplementary data

Supplementary data to this article can be found online at https://doi.org/10.1016/j.mtchem.2024.102375.

Data availability

Data will be made available on request.

References

[1] K. Sauer, P. Stoodley, D.M. Goeres, L. Hall-Stoodley, M. Burmølle, P.S. Stewart, T. Bjarnsholt, The biofilm life cycle: expanding the conceptual model of biofilm formation, Nat. Rev. Microbiol. 20 (2022) 608–620, https://doi.org/10.1038/s41579-022-00767-0.

[2] Z. Khatoon, C.D. McTiernan, E.J. Suuronen, T.F. Mah, E.I. Alarcon, Bacterial biofilm formation on implantable devices and approaches to its treatment and prevention, Heliyon 4 (2018) e01067, https://doi.org/10.1016/J.HELIYON.2018.E01067.

[3] R. Srinivasan, S. Santhakumari, P. Poonguzhali, M. Geetha, M. Dyavaiah, L. Xiangmin, Bacterial biofilm inhibition: a focused review on recent therapeutic strategies for combating the biofilm mediated infections, Front. Microbiol. 12 (2021) 676458, https://doi.org/10.3389/FMICB.2021.676458/BIBTEX.

[4] M. Cámara, W. Green, C.E. MacPhee, P.D. Rakowska, R. Raval, M.C. Richardson, J. Slater-Jefferies, K. Steventon, J.S. Webb, Economic significance of biofilms: a multidisciplinary and cross-sectoral challenge, Npj Biofilms and Microbiomes 8 (1) (2022) 1–8, https://doi.org/10.1038/s41522-022-00306-y, 8 (2022).

[5] G.M. Abebe, The role of bacterial biofilm in antibiotic resistance and food contamination, Internet J. Microbiol. 2020 (2020) 1705814, https://doi.org/10.1155/2020/1705814.

[6] F. Villa, F. Cappitelli, Plant-derived bioactive compounds at sub-lethal concentrations: towards smart biocide-free antibiofilm strategies, Phytochemistry Rev. 12 (2013) 245–254, https://doi.org/10.1007/S11101-013-9286-4.

[7] G. Annunziato, Strategies to overcome antimicrobial resistance (amr) making use of non-essential target inhibitors: a review, Int. J. Mol. Sci. 20 (2019) 5844, https://doi.org/10.3390/IJMS20235844.

[8] S. Buroni, L.R. Chiarelli, Antivirulence compounds: a future direction to overcome antibiotic resistance? Future Microbiol. 15 (2020) 299–301, https://doi.org/10.2217/fmb-2019-0294.

[9] S. Dell'orto, C. Cattò, F. Villa, F. Forlani, E. Vassallo, M. Morra, F. Cappitelli, S. Villa, A. Gelain, Low density polyethylene functionalized with antibiofilm compounds inhibits Escherichia coli cell adhesion, J. Biomed. Mater. Res. 105 (2017) 3251–3261, https://doi.org/10.1002/JBM.A.36183.

[10] F. Villa, W. Remelli, F. Forlani, A. Vitali, F. Cappitelli, Altered expression level of Escherichia coli proteins in response to treatment with the antifouling agent zosteric acid sodium salt, Environ. Microbiol. 14 (2012) 1753–1761, https://doi.org/10.1111/J.1462-2920.2011.02678.X.

[11] F. Rossi, C. Cattò, G. Mugnai, F. Villa, F. Forlani, Effects of the quinone oxidoreductase WrbA on Escherichia coli biofilm formation and oxidative stress, Antioxidants 10 (2021) 919, https://doi.org/10.3390/ANTIOX10060919.

[12] C. Cattò, G. James, F. Villa, S. Villa, F. Cappitelli, Zosteric acid and salicylic acid bound to a low density polyethylene surface successfully control bacterial biofilm formation, Biofouling 34 (2018) 440–452, https://doi.org/10.1080/08927014.2018.1462342.

[13] A.A. Nayl, A.I. Abd-Elhamid, A.A. Aly, S. Bräse, Recent progress in the applications of silica-based nanoparticles, RSC Adv. 12 (2022) 13706–13726, https://doi.org/10.1039/D2RA01587K.

[14] Y. Huang, P. Li, R. Zhao, L. Zhao, J. Liu, S. Peng, X. Fu, X. Wang, R. Luo, R. Wang, Z. Zhang, Silica nanoparticles: biomedical applications and toxicity, Biomed. Pharmacother. 151 (2022) 113053, https://doi.org/10.1016/J.BIOPHA.2022.113053.

[15] T.I. Janjua, Y. Cao, F. Kleitz, M. Linden, C. Yu, A. Popat, Silica nanoparticles: a review of their safety and current strategies to overcome biological barriers, Adv. Drug Deliv. Rev. 203 (2023) 115115, https://doi.org/10.1016/J.ADDR.2023.115115.

[16] V. Selvarajan, S. Obuobi, P.L.R. Ee, Silica nanoparticles—a versatile tool for the treatment of bacterial infections, Front. Chem. 8 (2020) 526915, https://doi.org/10.3389/FCHEM.2020.00602/BIBTEX.

[17] A. Bernardos, E. Piacenza, F. Sancenón, M. Hamidi, A. Maleki, R.J. Turner, R. Martínez-Máñez, A. Bernardos, F. Sancenón, R. Martínez-Máñez, E. Piacenza, R. J. Turner, M. Hamidi, A. Maleki, Mesoporous silica-based materials with bactericidal properties, Small 15 (2019) 1900669, https://doi.org/10.1002/SMLL.201900669.

[18] S. Kanugala, S. Jinka, N. Puvvada, R. Banerjee, C. Ganesh Kumar, Phenazine-1-carboxamide functionalized mesoporous silica nanoparticles as antimicrobial coatings on silicone urethral catheters, Sci. Rep. 9 (2019) 6198, https://doi.org/10.1038/s41598-019-42722-9.

[19] A. Mishra, V.K. Pandey, B.S. Shankar, J.S. Melo, Spray drying as an efficient route for synthesis of silica nanoparticles-sodium alginate biohybrid drug carrier of doxorubicin, Colloids Surf. B Biointerfaces 197 (2021) 111445, https://doi.org/10.1016/J.COLSURFB.2020.111445.

[20] R. Bengalli, S. Ortelli, M. Blosi, A. Costa, P. Mantecca, L. Fiandra, In vitro toxicity of TiO2:SiO2 nanocomposites with different photocatalytic properties, Nanomaterials 9 (2019) 1041, https://doi.org/10.3390/NANO9071041.

[21] European Centre for Ecotoxicology and Toxicology of Chemicals, Synthetic Amorphous Silica (CAS No. 7631-86-9) (2006).

[22] C. Cattò, S. Dell'Orto, F. Villa, S. Villa, A. Gelain, A. Vitali, V. Marzano, S. Baroni, F. Forlani, F. Cappitelli, Unravelling the structural and molecular basis responsible for the anti-biofilm activity of zosteric acid, PLoS One 10 (2015) e0131519, https://doi.org/10.1371/JOURNAL.PONE.0131519.

[23] C. Cattò, G. Grazioso, S. Dell'Orto, A. Gelain, S. Villa, V. Marzano, A. Vitali, F. Villa, F. Cappitelli, F. Forlani, The response of Escherichia coli biofilm to salicylic acid, Biofouling 33 (2017) 235–251, https://doi.org/10.1080/08927014.2017.1286649.

[24] N. Fairley, V. Fernandez, M. Richard-Plouet, C. Guillot-Deudon, J. Walton, E. Smith, D. Flahaut, M. Greiner, M. Biesinger, S. Tougaard, D. Morgan, J. Baltrusaitis, Systematic and collaborative approach to problem solving using X-ray photoelectron spectroscopy, Appl. Surf. Sci. 5 (2021) 100112, https://doi.org/10.1016/J.APSADV.2021.100112.

[25] D.Y. Kwok, A.W. Neumann, Contact angle measurement and contact angle interpretation, Adv. Colloid Interface Sci. 81 (1999) 167–249, https://doi.org/10.1016/S0001-8686(98)00087-6.

[26] T.T. Chau, A review of techniques for measurement of contact angles and their applicability on mineral surfaces, Miner. Eng. 22 (2009) 213–219, https://doi.org/10.1016/J.MINENG.2008.07.009.

[27] A. Polo, M.V. Diamanti, T. Bjarnsholt, N. Høiby, F. Villa, M.P. Pedeferri, F. Cappitelli, Effects of photoactivated titanium dioxide nanopowders and coating on planktonic and biofilm growth of *Pseudomonas aeruginosa*, Photochem. Photobiol. 87 (2011) 1387–1394, https://doi.org/10.1111/j.1751-1097.2011.00972.x.

[28] C. Guilhen, C. Forestier, D. Balestrino, Biofilm dispersal: multiple elaborate strategies for dissemination of bacteria with unique properties, Mol. Microbiol. 105 (2017) 188–210, https://doi.org/10.1111/MMI.13698.

[29] E. Werner, F. Roe, A. Bugnicourt, M.J. Franklin, A. Heydorn, S. Molin, B. Pitts, P. S. Stewart, Stratified growth in Pseudomonas aeruginosa biofilms, Appl. Environ. Microbiol. 70 (2004) 6188–6196, https://doi.org/10.1128/AEM.70.10.6188-6196.2004.

[30] R. Wang, S. Bao, F. Liu, X. Jiang, Q. Zhang, B. Sun, M. Zhu, Wear behavior of light-cured resin composites with bimodal silica nanostructures as fillers, Mater. Sci. Eng. C 33 (2013) 4759–4766, https://doi.org/10.1016/J.MSEC.2013.07.039.

[31] Y. An, M. Chen, Q. Xue, W. Liu, Preparation and self-assembly of carboxylic acid-functionalized silica, J. Colloid Interface Sci. 311 (2007) 507–513, https://doi.org/10.1016/J.JCIS.2007.02.084.

[32] R.R.L. De Oliveira, D.A.C. Albuquerque, T.G.S. Cruz, F.M. Yamaji, F.L. Leite, in: Measurement of the Nanoscale Roughness by Atomic Force Microscopy: Basic Principles and Applications, in: Atomic Force Microscopy - Imaging, Measuring and Manipulating Surfaces at the Atomic Scale, IntechOpen, 2012. https://doi.org/10.5772/37583.

[33] E.C. Talibouya Ba, M.R. Dumont, P.S. Martins, R.M. Drumond, M.P.M. da Cruz, V. F. Vieira, Investigation of the effects of skewness R_{sk} and kurtosis R_{ku} on tribological behavior in a pin-on-disc test of surfaces machined by conventional milling and turning processes, Mater. Res. 24 (2021) e20200435, https://doi.org/10.1590/1980-5373-MR-2020-0435.

[34] S. Zheng, M. Bawazir, A. Dhall, H.E. Kim, L. He, J. Heo, G. Hwang, Implication of surface properties, bacterial motility, and hydrodynamic conditions on bacterial surface sensing and their initial adhesion, Front. Bioeng. Biotechnol. 9 (2021) 643722, https://doi.org/10.3389/FBIOE.2021.643722/BIBTEX.

[35] A.V. Singh, V. Vyas, R. Patil, V. Sharma, P.E. Scopelliti, G. Bongiorno, A. Podestà, C. Lenardi, W.N. Gade, P. Milani, Quantitative characterization of the influence of the nanoscale morphology of nanostructured surfaces on bacterial adhesion and biofilm formation, PLoS One 6 (2011) e25029, https://doi.org/10.1371/JOURNAL.PONE.0025029.

[36] S. Wu, S. Altenried, A. Zogg, F. Zuber, K. Maniura-Weber, Q. Ren, Role of the surface nanoscale roughness of stainless steel on bacterial adhesion and microcolony formation, ACS Omega 3 (2018) 6456–6464, https://doi.org/10.1021/ACSOMEGA.8B00769.

[37] M.R. von Rohr, G. Furrer, H. Brandl, Effect of iron and phosphate on bacterial cyanide formation determined by methemoglobin in two-dimensional gradient microcultivations, J. Microbiol. Methods 79 (2009) 71–75, https://doi.org/10.1016/J.MIMET.2009.08.008.

[38] M. Perullini, S. Dulhoste, F. Ribot, G. Pehau-Arnaudet, O.M.M. Bouvet, J. Livage, N. Nassif, Bacteria metabolic adaptation to oxidative stress: the case of silica, J. Biotechnol. 374 (2023) 80–89, https://doi.org/10.1016/J.JBIOTEC.2023.08.002.

[39] M.S. Christodoulou, F. Villa, A. Pinto, F. Cappitelli, Correlation between perturbation of redox homeostasis and antibiofilm capacity of phytochemicals at non-lethal concentrations, Antioxidants 11 (2022) 2451, https://doi.org/10.3390/ANTIOX11122451.

[40] W. Rhimi, B. Theelen, T. Boekhout, D. Otranto, C. Cafarchia, Malassezia spp. yeasts of emerging concern in fungemia, Front. Cell. Infect. Microbiol. 10 (2020) 370, https://doi.org/10.3389/FCIMB.2020.00370.

[41] M. Čáp, L. Váchová, Z. Palková, Reactive oxygen species in the signaling and adaptation of multicellular microbial communities, Oxid. Med. Cell. Longev. 2012 (2012), https://doi.org/10.1155/2012/976753.

[42] L. Guo, C. Zhang, G. Chen, M. Wu, W. Liu, C. Ding, Q. Dong, E. Fan, Q. Liu, Reactive oxygen species inhibit biofilm formation of Listeria monocytogenes,

Microb. Pathog. 127 (2019) 183–189, https://doi.org/10.1016/J.MICPATH.2018.11.023.
[43] S.L. Chua, Y. Ding, Y. Liu, Z. Cai, J. Zhou, S. Swarup, D.I. Drautz-Moses, S. C. Schuster, S. Kjelleberg, M. Givskov, L. Yang, Reactive oxygen species drive evolution of pro-biofilm variants in pathogens by modulating cyclic-di-GMP levels, Open Biol 6 (2016) 160162, https://doi.org/10.1098/RSOB.160162.
[44] M. Gambino, F. Cappitelli, Mini-review: biofilm responses to oxidative stress, Biofouling 32 (2016) 167–178, https://doi.org/10.1080/08927014.2015.1134515.
[45] M. Čáp, L. Štěpánek, K. Harant, L. Váchová, Z. Palková, Cell differentiation within a yeast colony: metabolic and regulatory parallels with a tumor-affected organism, Mol Cell 46 (2012) 436–448, https://doi.org/10.1016/J.MOLCEL.2012.04.001.
[46] M. Schieber, N.S. Chandel, ROS function in redox signaling and oxidative stress, Curr. Biol. 24 (2014) R453–R462, https://doi.org/10.1016/J.CUB.2014.03.034.
[47] M. Mori, Z. Zhang, A. Banaei-Esfahani, J. Lalanne, H. Okano, B.C. Collins, A. Schmidt, O.T. Schubert, D. Lee, G. Li, R. Aebersold, T. Hwa, C. Ludwig, From coarse to fine: the absolute Escherichia coli proteome under diverse growth conditions, Mol. Syst. Biol. 17 (2021) e9536, https://doi.org/10.15252/MSB.20209536.
[48] C. Cattò, L. Corte, L. Roscini, G. Cardinali, F. Villa, F. Cappitelli, Metabolomic and proteomic changes in Candida albicans biofilm in response to zosteric acid treatment, Int. J. Mol. Sci. 23 (2022) 14067, https://doi.org/10.3390/IJMS232214067/S1.
[49] K. Tripti, D. Sayantan, S. Shardendu, D.N. Singh, A.K. Tripathi, Potential for the uptake and removal of arsenic [as (V) and as (III)] and the reduction of as (V) to as (III) by Bacillus licheniformis (DAS1) under different stresses, Kor. J. Microbiol. Biotechnol. 42 (2014) 238–248, https://doi.org/10.4014/KJMB.1401.01004.
[50] J.A. Bosch, H.S. Brand, T.J.M. Ligtenberg, B. Bermond, J. Hoogstraten, A.V. Nieuw Amerongen, Psychological stress as a determinant of protein levels and salivary-induced aggregation of Streptococcus gordonii in human whole saliva, Psychosom. Med. 58 (1996) 374–382, https://doi.org/10.1097/00006842-199607000-00010.
[51] B. Soufi, K. Krug, A. Harst, B. Macek, Characterization of the E. coli proteome and its modifications during growth and ethanol stress, Front. Microbiol. 6 (2015) 103, https://doi.org/10.3389/FMICB.2015.00103.
[52] R. Njenga, J. Boele, Y. Öztürk, H.G. Koch, Coping with stress: how bacteria fine-tune protein synthesis and protein transport, J. Biol. Chem. 299 (2023) 105163, https://doi.org/10.1016/J.JBC.2023.105163.